Infrared spectroscopic survey of the quiescent medium of nearby clouds. II. Ice formation and grain growth in Perseus and Serpens

Madden, M.C.L.; Boogert, A.C.A.; Chiar, J.E.; Knez, C.; Pendleton, Y.J.; Tielens, A.G.G.M.; Yip, A.

The Astrophysical Journal, 930:2 (17pp), 2022 May 1 https://doi.org/10.3847/1538-4357/ac617d

Infrared Spectroscopic Survey of the Quiescent Medium of Nearby Clouds. II. Ice Formation and Grain Growth in Perseus and Serpens

M. C. L. Madden[1], A. C. A. Boogert[2,10], J. E. Chiar[3,9], C. Knez[4,5,10], Y. J. Pendleton[6], A. G. G. M. Tielens[4,7], and A. Yip[8]

[1] Department of Astronomy, Columbia University, New York, NY 10027, USA
[2] Institute for Astronomy, University of Hawaii, 2680 Woodlawn Drive, Honolulu, HI 96822, USA; aboogert@hawaii.edu
[3] SETI Institute, 189 Bernardo Av., Suite 200, Mountain View, CA 94043, USA
[4] Department of Astronomy, University of Maryland, College Park, MD 20742, USA
[5] Johns Hopkins University Applied Physics Laboratory, 11100 Johns Hopkins Road, Laurel, MD 20723, USA
[6] NASA Ames Research Center, Moffett Field, CA 94035, USA
[7] Leiden Observatory, Leiden University, P.O. Box 9513, 2300 RA Leiden, The Netherlands
[8] Johns Hopkins University, Baltimore, MD 21218, USA
Received 2021 December 19; revised 2022 March 19; accepted 2022 March 24; published 2022 April 28

Abstract

The properties of dust change during the transition from diffuse to dense clouds as a result of ice formation and dust coagulation, but much is still unclear about this transformation. We present 2–20 μm spectra of 49 field stars behind the Perseus and Serpens Molecular Clouds and establish relationships between the near-infrared continuum extinction (A_K) and the depths of the 9.7 μm silicate ($\tau_{9.7}$) and 3.0 μm H_2O ice ($\tau_{3.0}$) absorption bands. The $\tau_{9.7}/A_K$ ratio varies from large, diffuse interstellar medium-like values ($\sim$0.55), to much lower ratios ($\sim$0.26). Above extinctions of $A_K \sim 1.2$ ($A_V \sim 10$; Perseus, Lupus, dense cores) and $\sim$2.0 ($A_V \sim 17$; Serpens), the $\tau_{9.7}/A_K$ ratio is lowest. The $\tau_{9.7}/A_K$ reduction from diffuse to dense clouds is consistent with a moderate degree of grain growth (sizes up to $\sim$0.5 μm), increasing the near-infrared color excess (and thus A_K), but not affecting the ice and silicate band profiles. This grain growth process seems to be related to the ice column densities and dense core formation thresholds, highlighting the importance of density. After correction for Serpens foreground extinction, the H_2O ice formation threshold is in the range of $A_K = 0.31$–0.40 ($A_V = 2.6$–3.4) for all clouds, and thus grain growth takes place after the ices are formed. Finally, abundant CH_3OH ice ($\sim$21% relative to H_2O) is reported for 2MASSJ18285266+0028242 (Serpens), a factor of >4 larger than for the other targets.

Unified Astronomy Thesaurus concepts: Interstellar dust (836); Interstellar dust extinction (837)

Supporting material: figure set

1. Introduction

The properties of interstellar grains have long been known to be different in dense clouds compared to diffuse clouds. The most easily recognizable differences include the 3.4 μm aliphatic hydrocarbons absorption feature, which is only present in diffuse clouds (e.g., Pendleton 1994; Chiar et al. 1996), and ice absorption bands, which have only been reported toward dense clouds (e.g., Boogert et al. 2015). The absence of the 3.4 μm aliphatic hydrocarbons absorption feature is still not well understood. The growth of ice mantles is a consequence of extinction in the ultraviolet, reducing the effects of photodesorption, and larger densities, increasing gas–grain interactions (e.g., Hollenbach et al. 2009). Also, the optical and infrared interstellar extinction curve is flatter in dense clouds, with the ratio of total to selective extinction $R_V = A_V/E(B-V)$ increasing from values of $\sim$3.1 to 5.5 (e.g., Indebetouw et al. 2005; McClure 2009). Deeper into the cloud ($A_V \sim 20$), increased flattening continues (Cambrésy et al. 2011). This is consistent with a reduction of the number density of the smallest grains (<0.1 μm), but does not necessarily trace growth of the largest grains (Weingartner & Draine 2001). Very large grains (>1 μm) were found to be associated with dense clouds, however, causing "coreshine" at wavelengths of 3.6 μm (Pagani et al. 2010). While it is observationally and theoretically well established that ice mantles are formed at relatively shallow dense cloud depths ($A_V \sim 1.6$, or observationally at $A_V \sim 3.2$ when both the front and the back of the clouds are traced), the thickness of ice mantles is limited to 5 nm by the available oxygen budget (e.g., Hollenbach et al. 2009). Therefore, coagulation of small grains, likely aided by sticky ice-coated grains, must govern the grain growth process (Ormel et al. 2011).

A sensitive indicator of the different dust properties in dense versus diffuse clouds is the depth of the 9.7 μm band of silicates ($\tau_{9.7}$) relative to the near-infrared continuum extinction (A_K). A reduction of $\tau_{9.7}/A_K$ in dense clouds by up to a factor of 2 was observed toward a range of sight-lines tracing nearby clouds and cores (Chiar et al. 2007), isolated dense cores (Boogert et al. 2011), and the Lupus Cloud (Boogert et al. 2013). Models suggest that this change is likely caused by grain growth affecting the near-infrared more than the silicate band, because the 9.7 μm band profile shows little variation (Van Breemen et al. 2011). Coagulation models of mixtures of

[9] Current address: Diablo Valley College, 321 Golf Club Road, Pleasant Hill, CA 94523, USA.
[10] Visiting Astronomer at the Infrared Telescope Facility, which is operated by the University of Hawaii under contract 80HQTR19D0030 with the National Aeronautics and Space Administration.

ice-coated graphite and silicate grains confirm this (Ormel et al. 2011).

The $\tau_{9.7}/A_K$ ratio and the 3.0 μm ice band optical depth ($\tau_{3.0}$) are interesting observational probes of the evolution of dust from diffuse to dense clouds. Following Ormel et al. (2011), it is expected that ice formation and grain growth are correlated. Observations generally agree with that expectation but, perhaps, not in all lines of sight (Boogert et al. 2013). It is the goal of this paper to further investigate the origin of the variations of the $\tau_{9.7}/A_K$ ratio. Following our papers on isolated dense cores (Boogert et al. 2011), and the Lupus Cloud (Boogert et al. 2013), here we study the $\tau_{9.7}/A_K$ ratio and ice abundances toward the Perseus and Serpens Molecular Clouds. These clouds are well studied, low-mass star-forming regions (Enoch et al. 2006; Jørgensen et al. 2006; Evans et al. 2009). With the Spitzer Infrared Array Camera (IRAC), the Legacy Project "From Molecular Clouds to Planet Forming Disks" (c2d; Evans et al. 2003, 2009) mapped 3.86 deg^2 of the Perseus molecular cloud and 0.89 deg^2 of the Serpens molecular cloud (Jørgensen et al. 2006; Harvey et al. 2006). We present Spitzer InfraRed Spectrograph (Spitzer/IRS), NASA InfraRed Telescope Facility SpeX (IRTF/SpeX), and Keck Near InfraRed SPECtrometer (Keck/NIRSPEC) *K*- and *L*-band spectra of background stars selected from this survey.

Throughout this paper we will assume Gaia-derived distances (Zucker et al. 2019) for the relevant clouds: 294 ± 15 pc for Perseus, 420 ± 15 pc for Serpens (Main; see also Ortiz-León et al. 2018), 189 ± 13 pc for Lupus, and 141 ± 7 pc for Taurus.

In Sections 2 and 3 respectively, the target selection and observation data are presented. In Section 4, the methods used to fit the spectra are given. Sections 5.1–5.4 show the correlations between the continuum extinction and the 9.7 μm silicate and 3.0 μm ice features. In Section 5.5, the CH_3OH abundances are analyzed. In Section 5.6, the results are put into a spatial context using maps of the extinction and the 3.5 μm broadband emission. In Sections 6.1 and 6.2 the results are compared to models of grain growth, and implications of the variations of the observed $\tau_{9.7}/A_K$ ratios are discussed. The results are also combined with those from previous works. The ice formation thresholds for the sample of clouds are compared in Section 6.3, and in Section 6.4 CH_3OH ice abundances are discussed. Finally, a summary including mention of future work is given in Section 7.

2. Source Selection

Background stars were selected from the Perseus and Serpens molecular clouds which were mapped with Spitzer/IRAC and MIPS by the c2d Legacy team (Evans et al. 2003, 2009). The maps are complete down to $A_V = 6$ and $A_V = 2$ for Serpens and Perseus, respectively (Evans et al. 2003). The selected sources have an overall spectral energy distribution (SED; 2MASS 1.2–2.2 μm, IRAC 3–8 μm, MIPS 24 μm) of a reddened Rayleigh–Jeans curve. They fall in the "star" category in the c2d catalogs and have MIPS 24 μm to IRAC 8 μm flux ratios greater than 4. In addition, fluxes are high enough (>10 mJy at 8.0 μm) to obtain Spitzer/IRS spectra of high quality (signal-to-noise ratio S/N > 50) within ~20 minutes of observing time per module. This resulted in a list of roughly 100 stars behind Perseus and 400 stars behind Serpens. The list was reduced by selecting ~10 sources in each interval of A_V of 2–5, 5–10, and >10 mag for Perseus, and 5–10, 10–15, and >15 mag for Serpens (taking A_V from the c2d catalogs) and making sure that the physical extent of the clouds is covered. For Serpens, there are more background stars to choose from and the overall extinction is higher, reflecting its lower Galactic latitude.

The final target list contains nearly all high A_V lines of sight. At low extinctions, many more sources were available and the brightest were selected. The observed samples of 28 targets toward Perseus and 21 toward Serpens are listed in Tables 1 and 2. The analysis shows that the SEDs of two Serpens sources cannot be fitted with stellar models (Section 5), because they likely have dust shells (silicate band emission). All other targets were found to be usable (hyper)giants or in a few cases main-sequence stars. One Perseus target (Per-16) was found to be a foreground rather than a background star. Reiners & Zechmeister (2020) measure a distance of 13.7 pc to Per-16, which is the closest target in our sample size by far. Indeed, we find no evidence for dust or ice extinction in this line of sight (Section 5.1).

Figures 1 and 2 plot the location of the observed background stars on extinction map contours derived from 2MASS and Spitzer photometry (Evans et al. 2009).

3. Observations

Spitzer/IRS spectra of background stars toward the Perseus and Serpens clouds were obtained as part of a dedicated Open Time program (PID 40580). Tables 1 and 2 list all sources with their astronomical observation request (AOR) keys and the IRS modules in which they were observed. The SL module, covering the 514 μm range, includes several ice absorption bands, as well as the 9.7 μm band of silicates, and has the highest signal-to-noise values (S/N > 50). The LL2 module (14–21 μm) was included in order to trace the 15 μm band of solid CO_2 and for a better overall continuum determination, although at a lower S/N of >30. At longer wavelengths, the background stars are weaker, and the LL1 module (~20–35 μm) was used for only ~30% of the sources. The spectra were extracted and calibrated from the two-dimensional Basic Calibrated Data produced by the standard Spitzer pipeline (version S16.1.0), using the same method and routines discussed in Boogert et al. (2011). Uncertainties (1σ) for each spectral point were calculated using the "func" frames provided by the Spitzer pipeline.

The Spitzer spectra of Perseus and a subset for Serpens were complemented by ground-based NASA IRTF/SpeX (Rayner et al. 2003) *K*- and *L*-band spectra. For the remaining Serpens targets, *L*-band spectra were obtained with the NIRSPEC spectrometer (McLean et al. 1998) on Keck II. The SpeX spectra were obtained in the LongXD1.9 or LongXD2.1 modes, offering wavelength ranges of 1.95–4.2 or 2.15–5.0 μm, respectively. The *M*-band portions of these spectra are only presented if they are of sufficiently high quality. The SpeX observations were done under observing programs 2008A079, 2008B074, and 2010A107 spread out over the nights listed in Tables 1 and 2. One target, Ser-7, was observed under program 2021A092 in the LXD_short mode (1.67–4.2 μm). For all SpeX observations, a slit width of 0.″3 was used, yielding a resolving power of $R = \lambda/\Delta\lambda = 2500$. The spectra were flat-fielded, wavelength-calibrated, and extracted using the Spextool package (Cushing et al. 2004). The telluric absorption lines were divided out and the spectra were flux-calibrated using the

Table 1
Perseus Target Observations

Alias[a] Per-	Name of Star 2MASS	Region[b]	Date[c] Ground-based	AOR key Spitzer/IRS	Modules[d]
1	03245605+3026005	LDN 1455 IRS 1	2008-09-27	23083008	SL, LL2
2	03261355+3029223	IRAS 03222+3034	2008-09-30	23085824	SL, LL2
3	03272467+3022547		2008-09-27	23083008	SL, LL2
4	03275729+3040138	LDN 1455 IRS 1	2008-09-30	23082752	SL, LL2
			2010-02-04		
			2010-02-05		
5	03281034+3026343	LDN 1455 IRS 1	2008-09-29*	23086336	SL, LL2
6	03290508+3022080	LDN 1455 IRS 1	2008-09-30	23087616	SL, LL2
7	03293654+3129465	NGC 1333	2008-09-25*	23088128	SL, LL2
8	03295603+3108454	NGC 1333	2008-09-30	23082752	SL, LL2
9	03300474+3023032	IRAS 03271+3013	2008-09-30	23086592	SL
10	03301239+3144408	NGC 1333	2008-09-28*	23086848	SL
11	03303022+3027087	IRAS 03271+3013	2008-09-25*	23087616	SL, LL2
12	03322030+3050485	IRAS 03292+3039	2008-09-25*	23088384	SL, LL2
13	03331023+3050177	IRAS 03292+3039	2008-09-26	23083776	SL, LL2
14	03332416+3117470		2008-09-29*	23087360	SL, LL2
15	03334078+3125007		2008-09-27	23083776	SL, LL2
			2010-02-05		
16	03360868+3118398		2008-09-25*	23084800	SL, LL2
17	03384753+3127345		2008-09-26*	23084032	SL, LL
18	03384901+3130173		2008-07-08*	23085312	SL, LL
19	03420993+3144139		2008-09-30	23086080	SL
20	03431627+3155097	IC 348	2010-02-05*	23087872	SL, LL2
21	03432386+3146110	IC 348	2008-09-26*	23085568	SL, LL2
22	03434808+3151030	IC 348	2008-09-28*	23084544	SL, LL2
			2008-09-29*		
23	03450207+3141196	IC 348	2008-09-27	23084544	SL, LL2
			2010-02-04		
			2010-02-05		
24	03450796+3204018	IC 348	2008-09-30	23084288	SL, LL2
25	03450839+3234202		2008-09-27	23083264	SL, LL2
			2010-02-04		
26	03452349+3158573	IC 348	2010-02-04	23083520	SL, LL2
			2010-02-05		
27	03465115+3238494		2008-09-26	23083264	SL, LL2
			2010-02-04		
28	03481723+3250595		2008-09-26*	23085568	SL, LL2

Notes.
[a] Alias used throughout this paper.
[b] Named location within the Perseus cloud, if available.
[c] Date of IRTF/SpeX observations. The instrument mode used is LongXD1.9 (1.95–4.2 μm), except for dates labeled with * for which it is LongXD2.1 (2.15–5.0 μm).
[d] Spitzer/IRS modules used: SL = Short-Low (5–14 μm, $R \sim 100$), LL2 = Long-Low 2 (14–21.3 μm, $R \sim 100$), LL = Long-Low 1 and 2 (14–35 μm, $R \sim 100$).

Xtellcor program (Vacca et al. 2003). Standard stars of spectral type A0V were used for this purpose.

The Keck/NIRSPEC spectra of the Serpens targets were observed in the long-slit mode with the 0.″57 wide slit, resulting in a resolving power of $R = 1500$. Two grating settings were observed, providing a full L-band coverage (2.83–4.2 μm). The data were reduced from the raw frames in a way standard for ground-based long-slit spectra with the same IDL routines described in Boogert et al. (2008). Sky emission lines were used for the wavelength calibration and bright, nearby main-sequence stars were used as telluric and photometric standards. For the division over the standard star, the S/N was optimized by carefully matching the wavelength scale to that of the science targets.

In the end, all SpeX, NIRSPEC, and Spitzer spectra were combined with 2MASS J, H, and K_s broadband photometry (Skrutskie et al. 2006), 3.55, 4.49, 5.73, and 7.87 μm photometry from c2d Spitzer/IRAC, 24 μm photometry from Spitzer/MIPS (Evans et al. 2003), and WISE photometry (Wright et al. 2010). The 1–5 μm spectra were matched to the photometry by convolving them with the K_s-band filter profile and then multiplying them along the flux scale. Similarly, the Spitzer/IRS spectra were matched to the IRAC 7.87 μm photometric flux. The same photometry was used in the continuum determination discussed in Section 4. Catalog flags were taken into account, such that the photometry of sources listed as being confused within a 2″ radius or being located within 2″ of a mosaic edge were treated as upper limits. The c2d catalogs do not include flags for saturation. Therefore, photometry exceeding the IRAC saturation limit (at the appropriate integration times) was flagged as a lower limit. In those cases, the nearby WISE photometric points were used instead. Finally, as the relative photometric calibration is important for this work, the uncertainties in the Spitzer c2d and

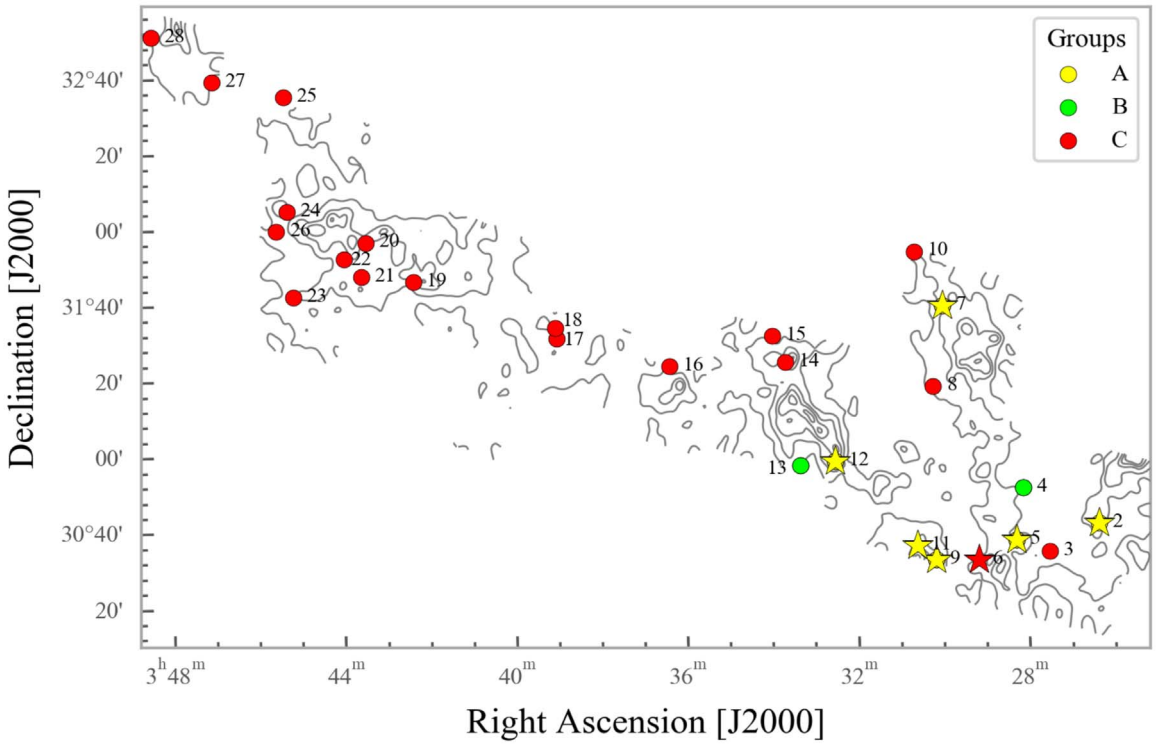

Figure 1. Perseus target positions labeled by alias and overlaid on extinction contours (Evans et al. 2009). The contours represent A_V extinction levels of 3, 6, 12, 18, and 24 mag. The target colors refer to the groupings determined in Section 5.1. Star symbols represent lines of sight with a 3.0 μm ice band optical depth ($\tau_{3.0}$) larger than 0.5 within the uncertainties.

Table 2
Serpens Target Observations

Alias[a] Ser-	Name of Star 2MASS	Region[c]	Date	Instrument[d]	AOR key	Modules[e]
			Ground-based		Spitzer/IRS	
1	18275901+0002337		2009-10-11	NIRSPEC	23073536	SL, LL2
2	18282010+0029141	Ser/G3-G6	2009-10-11	NIRSPEC	23073792	SL, LL2
3	18282631+0052133		2009-10-11	NIRSPEC	23072768	SL, LL
4	18284038+0044503	Ser/G3-G6	2009-10-11	NIRSPEC	23074816	SL, LL2
5	18284139+0017460	[EGE2007] Bolo 7[b]	2008-07-09	SpeX	23074048	SL, LL2
6	18284797+0037431	Ser/G3-G6	2009-10-11	NIRSPEC	23074304	SL, LL2
7	18285266+0028242	Ser/G3-G6	2007-07-05	NIRSPEC	13460224	SL, LL2
			2021-07-27	SpeX		
8	18290316+0023090	[EGE2007] Bolo 7[b]	2009-10-11	NIRSPEC	23076352	SL, LL2
9	18290436+0116207	Core	2009-10-11	NIRSPEC	23074304	SL, LL2
10	18290479-0001301		2008-07-09	SpeX	13210112	SL, LL
11	18291546+0016422	[EGE2007] Bolo 7[b]	2008-07-09	SpeX	23075328	SL, LL
12	18291600+0109382	Core	2008-07-09	SpeX	23073024	SL, LL
13	18291619+0045143	Ser/G3-G6	2009-10-11	NIRSPEC	23073024	SL, LL
14	18291699+0037191		2009-10-11	NIRSPEC	23076096	SL, LL2
15	18292528+0003141		2009-10-11	NIRSPEC	23072768	SL, LL
16	18294108+0127449	Core	2009-10-11	NIRSPEC	23073536	SL, LL2
17	18295604+0104146	Core	2008-07-08	SpeX	23075328	SL, LL
18	18295940+0041007		2008-07-08	SpeX	23075584	SL, LL2
			2008-07-09			
19	18300085+0017069		2009-10-11	NIRSPEC	23072768	SL, LL
20	18300896+0114441	Core	2009-10-11	NIRSPEC	23074816	SL, LL2
21	18301220+0115341	Core	2008-07-08	SpeX	23075584	SL, LL2

Notes.
[a] Alias used throughout this paper.
[b] Enoch et al. (2007).
[c] Named location within the Serpens cloud, if available.
[d] Wavelength range covered is 2.83–4.15 μm for Keck/NIRSPEC and 2.15–5.0 μm for IRTF/SpeX
[e] Spitzer/IRS modules used: SL = Short-Low (5–14 μm, $R \sim 100$), LL2 = Long-Low 2 (14–21.3 μm, $R \sim 100$), LL = Long-Low 1 and 2 (14–35 μm, $R \sim 100$).

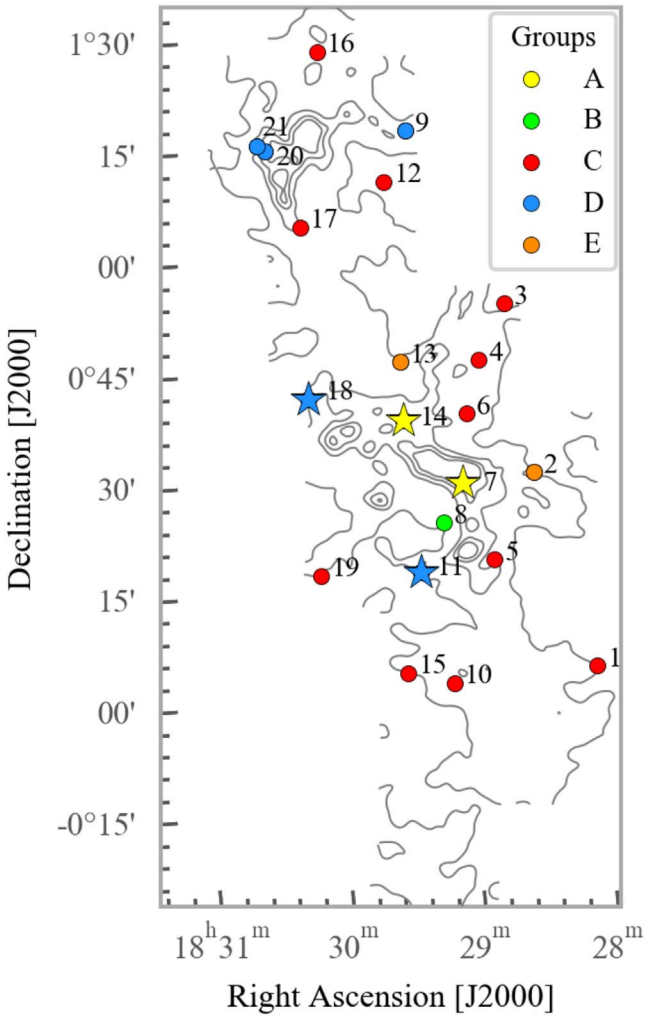

Figure 2. Serpens target positions overlaid on extinction contours (Evans et al. 2009). The contours represent A_V extinction levels of 3, 6, 12, 18, and 24 mag. The target colors refer to the groupings determined in Section 5.1. Star symbols represent lines of sight with an ice band optical depth $\tau_{3.0} > 0.5$ within the uncertainties.

2MASS photometry were increased with the zero-point magnitude uncertainties listed in Table 21 of Evans et al. (2009) and further discussed in Section 3.5.3 of that paper.

4. Methods

To determine the interstellar A_K, $\tau_{3.0}$, and $\tau_{9.7}$ values, contributions from the stellar photosphere to the observed spectra need to be removed. We did so, following the methods described in Boogert et al. (2011, 2013) and Chu et al. (2020). The fits to the observed spectra were significantly more constrained by combining the spectra with broadband photometric data (Section 3).

The fitting process was done in two steps. First, all data available in the 1–5 μm range were fitted using a large (224) database of template spectra (Rayner et al. 2009) to derive accurate spectral types, as well as A_K and $\tau_{3.0}$ values. Second, all data in the full 1–20 μm range were fitted using a small (13) sample of model spectra (Decin et al. 2004; Boogert et al. 2011) to provide $\tau_{9.7}$. Throughout this paper, the A_K and $\tau_{3.0}$ values derived from the 1–5 μm template fitting process are reported, as they are most accurate considering the much larger database of template spectra available.

All fit parameters are determined simultaneously, and any dependencies are taken into account in the uncertainty estimates. For the 1–5 μm template fits, this is described in detail in Chu et al. (2020). In short, the key fit parameters are as follows.

1. Spectral type. The CO overtone lines between 2.25–2.60 μm provide a sensitive tracer of spectral type. The near-infrared *JHK* photometry and absorption features in the 3.8–4.1 μm spectral range also prove to be important for this. The *JHK* photometry depends on the extinction as well, which is discussed in point 2.

2. Continuum extinction (A_K). We adopt the commonly used extinction curve from Indebetouw et al. (2005). Due to the steepness of the extinction curve in the 1.0–2.5 μm region, A_K and its uncertainty are primarily determined by the *JHK* photometry and the shape of the un-reddened spectral template spectrum. The dependency on flux values at longer wavelengths is weak.

3. H_2O absorption feature ($\tau_{3.0}$). H_2O ice has a prominent broad feature at 3.0 μm. $\tau_{3.0}$ and its uncertainty are determined by the flux values and the observational noise in the 2.9–3.2 μm range, including dependencies on the accuracy of the baseline surrounding the ice feature. For the fitting, an H_2O ice absorption spectrum for spherical, pure ice grains using optical constants of amorphous ice at a temperature of 10 K (Hudgins et al. 1993) is assumed. A grain size of 0.4 μm is chosen. This particular ice temperature and grain size have no significance other than that they match the shape of the 3.0 μm band well, providing a tool to derive $\tau_{3.0}$.

Besides the reduced χ^2 values derived for the individual wavelength regions discussed above, a total reduced χ^2 (χ^2_ν) is calculated across the wavelength range of 1–4 μm, using the IRTF template database. Where this χ^2_ν is lowest, the model template is chosen as the best fit to the star. The final errors for A_K and $\tau_{3.0}$ are increased by including all of the model templates that have χ^2_ν (1–4 μm) within a factor of 2 of the best template. This represents a confidence level of at least 3σ. In some cases, the uncertainties on A_K and $\tau_{3.0}$ are much smaller than expected from the χ^2_ν across the full 1–4 μm wavelength range, because A_K and $\tau_{3.0}$ depend strongly on only a subset of this wavelength range.

For the full 1–21 μm fits, using a much smaller set of stellar models, $\tau_{3.0}$ is kept fixed. The strength and shape of the longer-wavelength H_2O ice bands is set by assuming the H_2O ice model discussed above. The 9.7 μm silicate band is fitted for grains small compared to the wavelength, having a pyroxene to olivine optical depth ratio of 0.62 at the 9.7 μm peak (Boogert et al. 2011). A key factor in the fitting process is the photospheric SiO band at $\sim$8 μm, as it overlaps with the 9.7 μm band of silicate dust. For some targets, the model spectral types were optimized to fit that photospheric band best. Also, in some cases the models were normalized to the data at a wavelength of 8.0 μm, instead of the default of 5.5 μm. This provides a better local baseline for the silicate feature, while reducing the fit quality at other wavelengths. Accurate $\tau_{9.7}$ values are more important for this work than a good fit over the larger wavelength range.

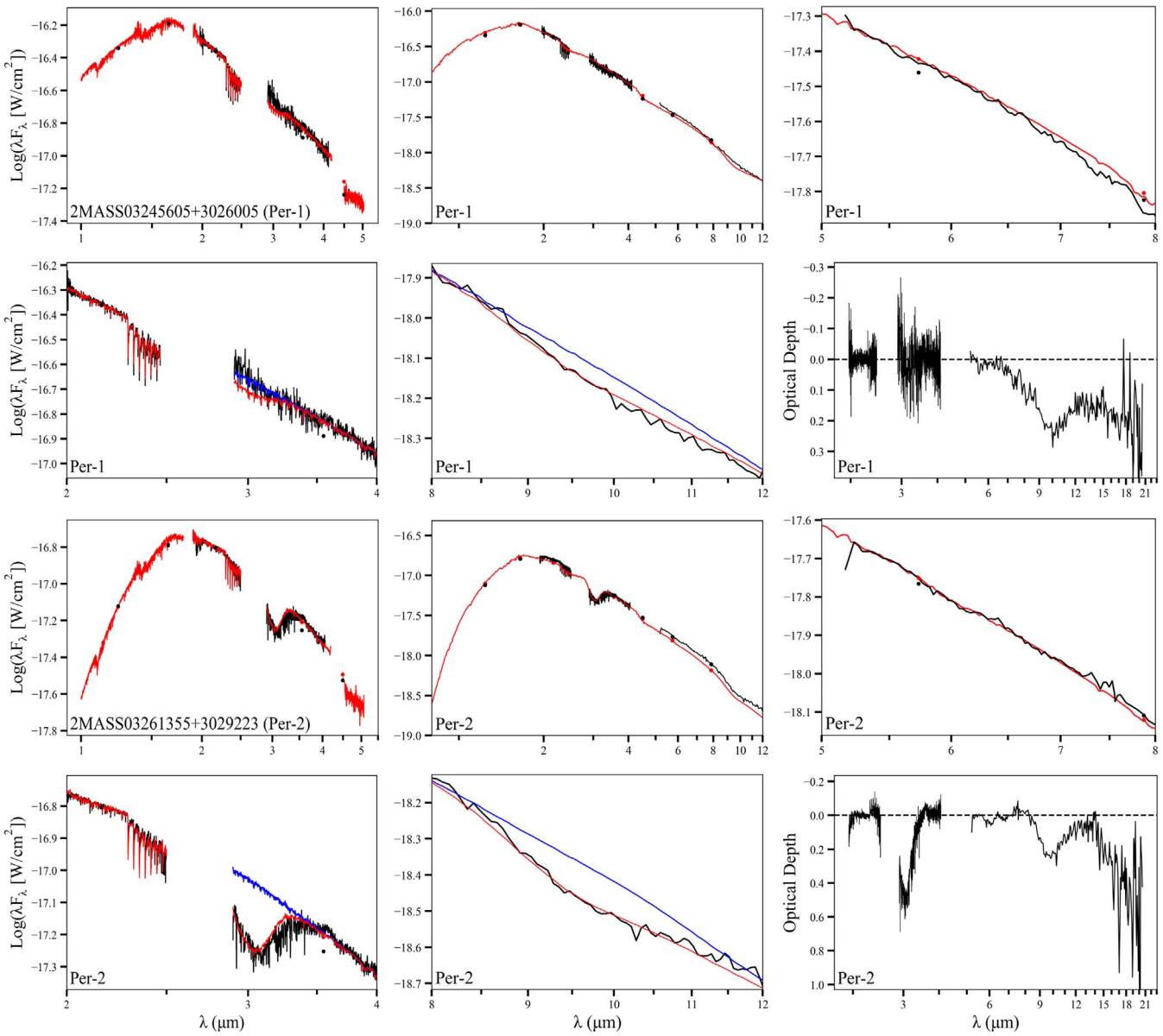

Figure 3. Model fits and optical depth plots of the 28 Perseus and 21 Serpens targets. Each target has a 2 × 6 format of its plots: short-wavelength IRTF model (top left), full-wavelength IRTF and Spitzer model (top middle), 5–8 μm (top right), 2–4 μm (bottom left), 8–12 μm (bottom middle), and optical depth (bottom right). Black indicates the observed data, and red the model data. The 2–4 μm plot indicates any presence of the 3 μm OH stretch mode, which is made more prominent by the blue model flux which has the H_2O ice contribution omitted; the models do not include parameters to fit the wings around 3.4 μm. The 8–12 μm plot indicates any presence of the 9.7 μm silicates, which is made more prominent by the blue model flux which has the silicates contribution omitted. The 5–8 μm plot indicates any presence of the 6 μm OH stretch mode and the 6.85 μm absorption feature due to, tentatively, NH_4^+. The complete figure set (17 images) is available in the online journal.

(The complete figure set (17 images) is available.)

5. Results

Using the models described in Section 4, the values for A_K, $\tau_{3.0}$, and $\tau_{9.7}$ are derived. The best-fitting models are shown in Figure 3 below and the derived values in Tables 3 and 4.

The fits to the 1–5 μm wavelength region, using the IRTF template database, are generally good. In a fair number of cases, however, we did notice deficiencies in fitting the continuum region near 4.0 μm, even though the data at shorter wavelengths were fitted well. This could be due to calibration errors in the slope of the 2–4 μm SpeX spectra or in the Spitzer or WISE photometry used to calibrate the NIRSPEC spectra (for which no *K*-band portion is available). It could also reflect an uncertainty in the extinction curve or incompleteness of the spectral database. Regardless of the origin, we reduced the effect on the derived $\tau_{3.0}$ by scaling the *L*-band spectrum to match the best-fitting model. The scaling factors are provided in Tables 3 and 4. In five cases, this correction factor is less than 5%, and in 23 cases 5%–17%. We are confident in the derived values of $\tau_{3.0}$, as the absorption band can be distinguished by the shape to the *L*-band spectrum, and the adjustments are essentially local baseline corrections.

Of all 49 targets, seven have deviating slopes in the 8–12 μm region, even though the IRTF template fits in the 1–5 μm range

Table 3
Perseus Target Results

Alias (Per-)	IRTF Template 1–5 μm	Model 1–30 μm	A_K mag	$\tau_{3.0}$	$\tau_{9.7}$	χ^2_ν	N(H_2O_{ice})[a] 10^{17}cm^{-2}	Notes
1	HD16068 (K3.5II)	K4III	0.34 ± 0.07	0.0 ± 0.12	0.26 ± 0.09	2.92	<1.94	L-band = 1.15
2	HD170820 (G9II)	K0III	0.92 ± 0.08	0.49 ± 0.17	0.23 ± 0.05	0.76	7.87 ± 2.73	L-band = 1.15
3	HD44391 (K0I)	K0III[b]	0.30 ± 0.08	0.01 ± 0.05	0.24 ± 0.07	0.57	<0.83	⋯
4	HD222093 (G9III)	G8III	0.22 ± 0.06	0.0 ± 0.05	0.22 ± 0.05	2.02	<0.81	L-band = 1.02
5	HD202314 (G6I)	G8III	1.27 ± 0.09	0.49 ± 0.06	0.33 ± 0.05	0.51	7.91 ± 0.97	L-band = 1.13
6	HD44391 (K0I)	G8III[b]	0.75 ± 0.07	0.39 ± 0.08	0.38 ± 0.05	1.70	6.29 ± 1.36	L-band = 0.93
7	HD35620 (K3.5III)	K4III	1.63 ± 0.05	0.55 ± 0.05	0.35 ± 0.05	0.24	8.97 ± 0.82	L-band = 0.97
8	HD44391 (K0I)	K0III[b]	0.43 ± 0.15	0.01 ± 0.11	0.26 ± 0.05	0.5	<1.78	L-band = 1.07
9	HD192713 (G3I)	G8III	1.41 ± 0.05	0.52 ± 0.05	0.41 ± 0.05	0.67	8.47 ± 0.86	L-band = 1.06
10	HD9852 (K0.5III)	K4III	1.32 ± 0.14	0.24 ± 0.08	0.57 ± 0.07	1.11	3.81 ± 1.27	⋯
11	HD132935 (K2III)	K5III	1.69 ± 0.07	0.84 ± 0.05	0.43 ± 0.05	1.24	13.66 ± 0.82	L-band = 1.07
12	HD182694 (G7III)	G8III	1.87 ± 0.12	0.92 ± 0.11	0.38 ± 0.07	1.11	14.9 ± 1.79	L-band = 0.92
13	HD9852 (K0.5III)	G8III[b]	0.21 ± 0.17	0.0 ± 0.05	0.19 ± 0.05	1.08	<0.81	⋯
14	HD91810 (K1III)	K3III	1.43 ± 0.05	0.29 ± 0.11	0.57 ± 0.09	0.81	4.76 ± 1.80	⋯
15	HD120477 (K5.5III)	K7III	0.42 ± 0.11	0.0 ± 0.10	0.24 ± 0.08	3.24	<1.62	L-band = 1.03
16	Gl581 (M2.5V)	G8III	0.0 ± 0.05	0.09 ± 0.05	0.0 ± 0.05	3.65	1.41 ± 0.78	L-band = 0.93
17	HD35620 (K3.5III)	K7III[b]	0.67 ± 0.12	0.08 ± 0.05	0.29 ± 0.07	0.59	1.32 ± 0.82	L-band = 0.95
18	HD213893 (M0III)	K4III	0.58 ± 0.09	0.04 ± 0.05	0.24 ± 0.06	0.71	<0.84	L-band = 0.98
19	HD108519 (F0V)	G8III	0.98 ± 0.05	0.18 ± 0.06	0.35 ± 0.07	1.17	2.91 ± 0.97	local 9.7 μm baseline
20	HD160365 (F6III)	G8III	1.23 ± 0.13	0.1 ± 0.06	0.54 ± 0.06	4.09	1.63 ± 0.98	L-band = 0.95
21	HD222093 (G9III)	G8III[b]	0.95 ± 0.08	0.06 ± 0.05	0.34 ± 0.05	0.68	0.97 ± 0.81	L-band = 0.98
22	HD4408 (M4III)	M6III	0.95 ± 0.06	0.19 ± 0.05	0.33 ± 0.08	2.99	3.01 ± 0.79	L-band = 0.83, local 9.7 μm baseline
23	HD132935 (K2III)	K4III	0.71 ± 0.1	0.13 ± 0.08	0.37 ± 0.05	0.80	2.09 ± 1.29	L-band = 0.90
24	HD10697 (G3V)	G8III	0.61 ± 0.11	0.09 ± 0.09	0.27 ± 0.05	1.18	1.49 ± 1.49	L-band = 0.95
25	HD100006 (K0III)	K0III	0.35 ± 0.09	0.0 ± 0.06	0.12 ± 0.05	1.77	<0.97	⋯
26	HD16139 (G8.5III)	G8III	0.49 ± 0.09	0.04 ± 0.05	0.20 ± 0.05	0.89	<0.83	⋯
27	HD132935 (K2III)	K3III	0.37 ± 0.05	0.05 ± 0.05	0.22 ± 0.05	0.49	0.83 ± 0.83	⋯
28	HD35620 (K3.5III)	K4III[b]	0.76 ± 0.12	0.23 ± 0.11	0.26 ± 0.05	0.51	3.72 ± 1.78	L-band = 0.95

Notes. Perseus targets observed by alias along with the fitted IRTF templates, full spectra templates assuming spectral types, extinctions, water ice optical depths, silicate optical depths, χ^2_ν values for the IRTF template database fits, water ice column densities, and extra notes ("L-band" indicates the L-band flux scaling factor).
[a] Column density upper limits are 3σ.
[b] Poor fit 8 μm photospheric SiO band.

are good. This may reflect the small number of 1–20 μm photospheric models available. In order to improve the fit of the 9.7 μm silicate feature, a local baseline correction was applied by changing the wavelength range for which the model is normalized to the observations from the default of 5.34–5.50 μm to 7.3–7.5 μm. However, for two of these targets (Ser-2 and Ser-13), this approach was insufficient. The deviations from the model were very large, and there was a hint of silicate emission affecting the shape of the 9.7 μm absorption feature. For these, probably more evolved, mass-losing stars, we discarded the derived $\tau_{9.7}$ values. For another 10 targets, while the 8–12 μm slopes were in good agreement with the spectral types derived from the 1–5 μm range, the 8 μm SiO photospheric absorption band suggested later spectral types. Such inconsistency was also noted for several Lupus background stars (Boogert et al. 2013). The affected targets are indicated in Tables 3 and 4, and the effect on the reported $\tau_{9.7}$ values was taken into account.

5.1. $\tau_{9.7}$ and A_K Correlation

Analogous to earlier work (Chiar et al. 2007; Boogert et al. 2013), we plot the derived values for $\tau_{9.7}$ against A_K (Figure 4). The rising trend is fitted with

$$\tau_{9.7} = m \times A_K. \quad (1)$$

We find that for Perseus, $m = 0.416 \pm 0.026$, and for Serpens, $m = 0.406 \pm 0.041$. A significant amount of scatter is visible in these plots, especially for Perseus. In order to investigate the origin of these variations, we separate the target into different groups. Throughout this work, we will refer to these as Groups A to E.

The targets that fall at least 6σ below the linear fit are referred to as "Group A." Those that are at least 6σ above this relation will be referred to as "Group B." As can be seen in Figure 4, Group A targets follow the Lupus IV dense cloud relation ($m = 0.26$; Boogert et al. 2013), and Group B targets follow the diffuse interstellar medium (ISM) relation ($m = 0.554$; Whittet 2003). Based on this, targets that fall within 6σ of more than one of these three relations are assigned to "Group C," and targets that exclusively follow the fits over all targets are in "Group D." Only Serpens exhibits this latter Group. For Perseus, several Group C targets follow the overall fit, but the uncertainties are too large to assign them to Group D. Finally, targets for which no reliable $\tau_{9.7}$ values could be derived, but that do have A_K and $\tau_{3.0}$ measurements, are in "Group E." Also, note that one target (Per-16) has

Table 4
Serpens Target Results

Alias (Ser-)	IRTF Template 1–5 μm	Model 1–30 μm	A_K mag	$\tau_{3.0}$	$\tau_{9.7}$	χ^2_ν	N(H_2O_{ice})[a] 10^{17}cm^{-2}	Notes
1	HD204724 (M1III)	M1III[c]	0.73 ± 0.23	0.10 ± 0.10	0.24 ± 0.05	0.86	1.64 ± 1.64	⋯
2	HD196610 (M6III)	M7III	0.87 ± 0.16	0.10 ± 0.18	⋯[b]	1.25	<2.93	⋯
3	HD179870 (K0II)	K3III[c]	0.75 ± 0.19	0.03 ± 0.06	0.31 ± 0.05	1.91	<0.97	L-band = 0.95
4	HD28487 (M3.5III)	M3III	1.12 ± 0.17	0.24 ± 0.12	0.38 ± 0.08	1.18	3.81 ± 1.91	⋯
5	HD64332 (S4.5)	M1III	1.09 ± 0.07	0.22 ± 0.08	0.36 ± 0.05	0.24	3.62 ± 1.32	L-band = 1.10
6	HD4408 (M4III)	M1III	1.01 ± 0.05	0.21 ± 0.09	0.44 ± 0.07	0.64	3.32 ± 1.42	local 9.7 μm baseline
7	HD18191 (M6III)	M6III	4.75 ± 0.44	1.63 ± 0.06	1.18 ± 0.06	0.87	26.33 ± 0.97	L-band = 1.10, local 9.7 μm baseline
8	HD4408 (M4III)	M6III	0.73 ± 0.05	0.09 ± 0.05	0.42 ± 0.05	0.64	1.52 ± 0.85	⋯
9	HD201065 (K4I)	M0III	0.92 ± 0.40	0.08 ± 0.07	0.37 ± 0.05	1.01	1.38 ± 1.20	⋯
10	HD39045 (M3III)	M1III	0.73 ± 0.08	0.13 ± 0.13	0.31 ± 0.05	0.26	2.18 ± 2.18	L-band = 0.95
11	HD204724 (M1III)	M6III	1.44 ± 0.12	0.47 ± 0.13	0.54 ± 0.05	0.48	7.66 ± 2.12	⋯
12	HD204724 (M1III)	M0III	0.71 ± 0.13	0.03 ± 0.11	0.19 ± 0.06	3.03	<1.81	L-band = 1.10
13	HD194193 (K7III)	M1III	0.78 ± 0.15	0.05 ± 0.12	⋯[b]	0.94	<2.02	L-band = 1.15
14	HD4408 (M4III)	M6III	2.03 ± 0.09	0.63 ± 0.20	0.61 ± 0.09	0.89	10.16 ± 3.22	local 9.7 μm baseline
15	HD201065 (K4I)	K7III[c]	0.69 ± 0.33	0.03 ± 0.05	0.29 ± 0.08	0.81	<0.82	⋯
16	HD201065 (K4I)	M1III	0.83 ± 0.24	0.06 ± 0.07	0.28 ± 0.08	1.13	<1.15	⋯
17	HD94705 (M5.5III)	M6III	1.40 ± 0.05	0.08 ± 0.18	0.54 ± 0.13	0.39	<2.88	⋯
18	HD108477 (G4III)	G8III	1.91 ± 0.20	0.50 ± 0.05	0.74 ± 0.06	0.54	8.13 ± 0.81	L-band = 1.08
19	HD11443 (F6IV)	G8III	0.98 ± 0.24	0.0 ± 0.05	0.43 ± 0.06	3.50	<0.81	⋯
20	HD28487 (M3.5III)	M6III	1.19 ± 0.15	0.24 ± 0.12	0.43 ± 0.05	0.93	3.87 ± 1.94	⋯
21	HD44391 (K0I)	G8III	1.61 ± 0.10	0.29 ± 0.05	0.57 ± 0.05	0.48	4.63 ± 0.80	L-band = 1.07

Notes. Serpens targets observed by alias along with the fitted IRTF templates, full spectra templates assuming spectral types, extinctions, water ice optical depths, silicate optical depths, the total reduced χ^2_ν values for the IRTF template database fits, water ice column densities, and extra notes ("L-band" indicates the L-band flux scaling factor).
[a] Column density upper limits are 3σ.
[b] Poor full spectrum fit, resulting in discarded $\tau_{9.7}$ value.
[c] Poor fit 8 μm photospheric SiO band.

$A_K = 0.0 \pm 0.05$ (Table 3), which is consistent with its distance of 13.7 pc (Reiners & Zechmeister 2020), indicating this target is actually a Perseus foreground, rather than background, star.

5.2. $\tau_{3.0}$ and A_K Correlation

The relation between $\tau_{3.0}$ and A_K can be used to determine the ice formation threshold (e.g., Whittet et al. 2001) and to determine the abundance of ices relative to dust. This relation is plotted for Perseus and Serpens in Figure 5. Generally, $\tau_{3.0}$ increases as a function of A_K, and the relation does not go through the origin. The data points are therefore fitted with the function

$$\tau_{3.0} = a \times A_K + b. \quad (2)$$

We find that for Perseus, $a = 0.430 \pm 0.054$ and $b = -0.136 \pm 0.052$, and for Serpens, $a = 0.391 \pm 0.021$ and $b = -0.241 \pm 0.032$. The abscissa of this relation gives the ice formation threshold. For Perseus this is $A_K = 0.315 \pm 0.127$, and for Serpens $A_K = 0.616 \pm 0.087$. The Perseus values are comparable to those for Lupus IV: $a = 0.44 \pm 0.03$ and $b = -0.11 \pm 0.03$, and an ice formation threshold of $A_K = 0.25 \pm 0.07$ (Boogert et al. 2013). The Serpens ice formation threshold is almost twice that of the other clouds, which may relate to unrelated foreground extinction at the larger distance of Serpens (Section 6.3; Zucker et al. 2019).

For Perseus, $\tau_{3.0}$ shows a significant scatter as a function of A_K (Figure 5(a)). By indicating the different groups identified in the $\tau_{9.7}$ versus A_K correlation (Section 5.1), it is evident that the Group A targets, i.e., those with the most suppressed, "dense core-like" silicate bands, have deeper water ice bands at a given A_K than the Group C targets. These Group A targets closely follow the Taurus ice correlation, within 3σ ($a = 0.60 \pm 0.02$, $b = -0.23 \pm 0.01$; Whittet et al. 2001).

For Serpens (Figures 5(b) and (c)), all targets have $\tau_{3.0}$ values that fall significantly below the Taurus correlation. This is not only reflected in the higher-extinction threshold derived above, but also in the shallower slope of the correlation. The latter might indicate lower H_2O ice abundances in Serpens compared to Taurus. It might also be a reflection of smaller grain sizes in Serpens, enhancing A_K relative to $\tau_{3.0}$ (Section 6.1). Here again, the different groups, distinguished in the $\tau_{9.7}$ versus A_K correlation, are indicated. All groups follow the same correlation, but Group A targets are higher on the correlation than Group C and D targets. It is also worth noting that all targets, with the exception of Ser-19 (Group C), have H_2O ice detections, including the Group B "diffuse ISM" target Ser-8.

5.3. $\tau_{3.0}$ and $\tau_{9.7}$ Correlation

The relations between $\tau_{3.0}$ and $\tau_{9.7}$ (Figure 6) are linear, although they are distinctly different for Serpens and Perseus. Least-squares fits yield for Perseus

$$\tau_{9.7} = (0.21 \pm 0.09) \times \tau_{3.0} + (0.26 \pm 0.03) \quad (3)$$

and for Serpens

$$\tau_{9.7} = (0.55 \pm 0.06) \times \tau_{3.0} + (0.31 \pm 0.03). \quad (4)$$

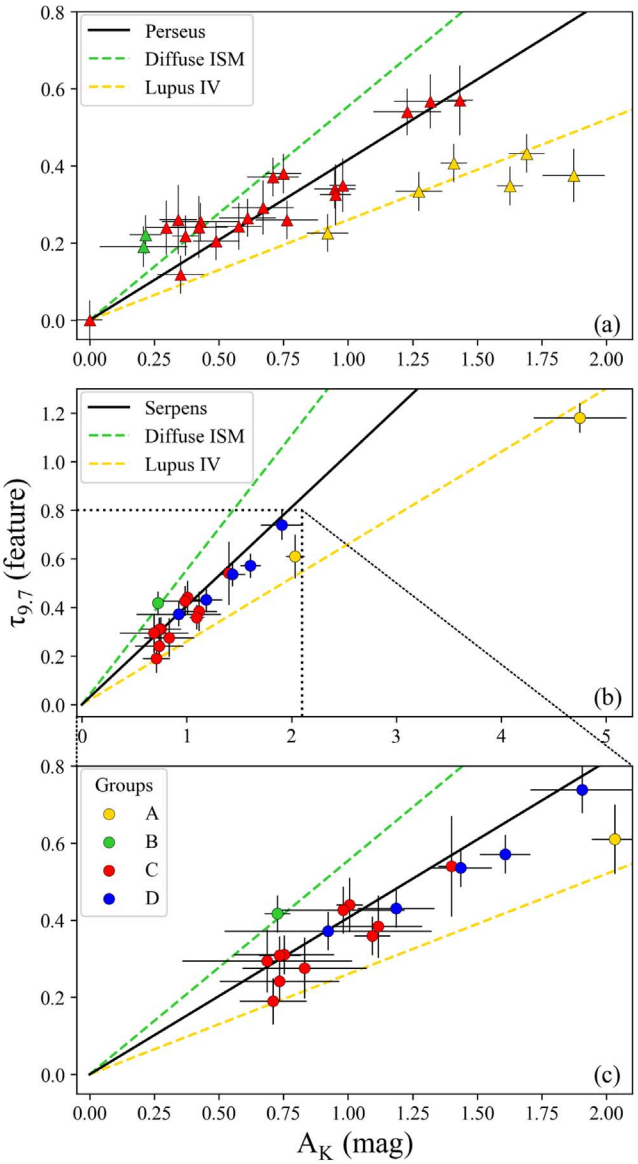

Figure 4. Silicate band optical depth and extinction correlation for Perseus (a) and Serpens ((b) and (c)) targets. The error bars are of 3σ significance. The solid black line is a least-squares fit to all targets in the cloud. The dashed yellow line is the Lupus IV correlation from Boogert et al. (2013). The dashed green line is the diffuse interstellar medium (ISM) correlation from Whittet (2003). Panel (c) zooms in on the lower-extinction Serpens targets. The colors of the bullets represent the groups defined in Section 5.1, and are indicated in panel (c). They apply to panels (a) and (b) as well as to the other figures in this paper.

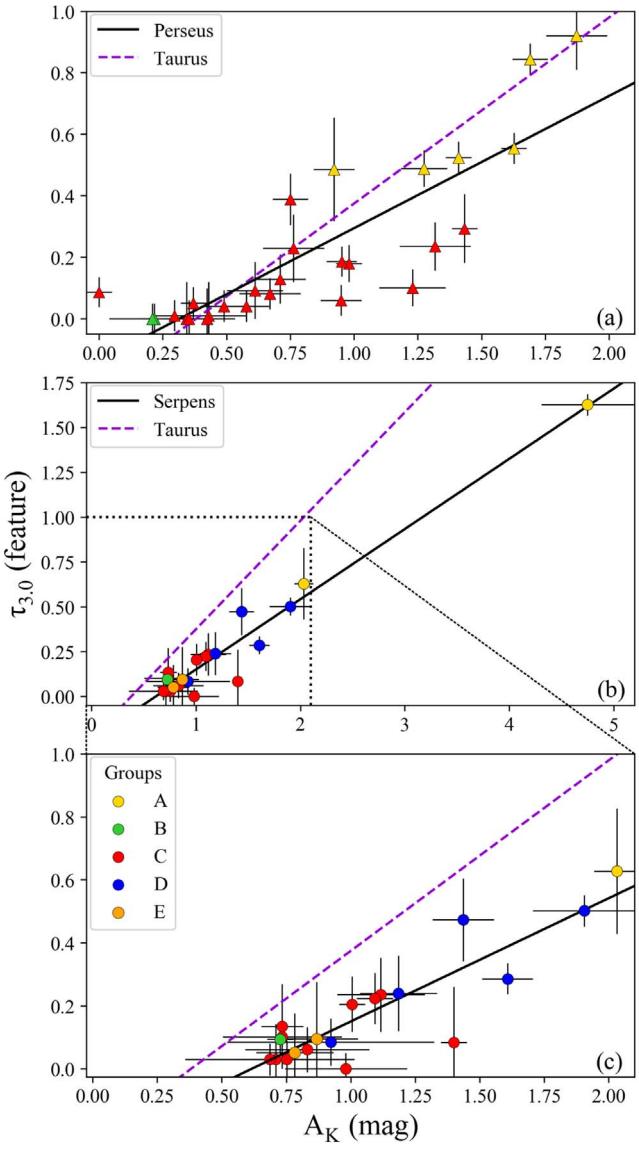

Figure 5. Water ice band optical depth and extinction correlations for Perseus (a) and Serpens ((b) and (c)) targets. The error bars are of 3σ significance. The solid black line is a least-squares fit to all targets in the cloud. The dashed purple line is the Taurus molecular cloud correlation from Whittet et al. (2001). The colors of the data points correspond to the groupings defined in Section 5.1 and Figure 4. Panel (c) zooms in on the lower-extinction Serpens targets.

For comparison, the relation in a sample of isolated dense cores (Boogert et al. 2011) is

$$\tau_{9.7} = (0.36 \pm 0.06) \times \tau_{3.0} + (0.36 \pm 0.09). \quad (5)$$

The relation is significantly steeper in Serpens compared to Perseus. In fact, for $\tau_{3.0} > 0.15$ the Perseus relation is almost flat, i.e., while $\tau_{3.0}$ increases with a factor of 5, and $\tau_{9.7}$ increases by at most a factor of 1.5. Also, compared to the dense cores, the Perseus $\tau_{9.7}$ values are systematically a factor of 2 lower. The Serpens relation is in better agreement with that of dense cores (Boogert et al. 2011), although the slope in Serpens is steeper.

5.4. $\tau_{9.7}/A_K$ and $\tau_{3.0}$ Correlation

The Group A targets are well separated from the other groups along the $\tau_{3.0}$ axis in Figure 6. This is confirmed in the relations between $\tau_{9.7}/A_K$ and $\tau_{3.0}$ (Figure 7), where the Group A targets have the lowest $\tau_{9.7}/A_K$ ratios and the largest $\tau_{3.0}$ values. This trend is also visible for Lupus. The isolated dense cores are biased to the highest A_K and $\tau_{3.0}$ values. The group of points with the higher $\tau_{9.7}/A_K$ ratios are from the core L328, which has a known diffuse dust foreground component.

5.5. CH_3OH Ice

A number of targets show ice absorption features in the 5–20 μm wavelength range, most commonly the 6 μm O–H bending mode of H_2O. Three of them, two behind Perseus and one behind Serpens, show particularly deep ice absorption features (Figure 8). The 9.7 μm CO stretch mode arising from CH_3OH

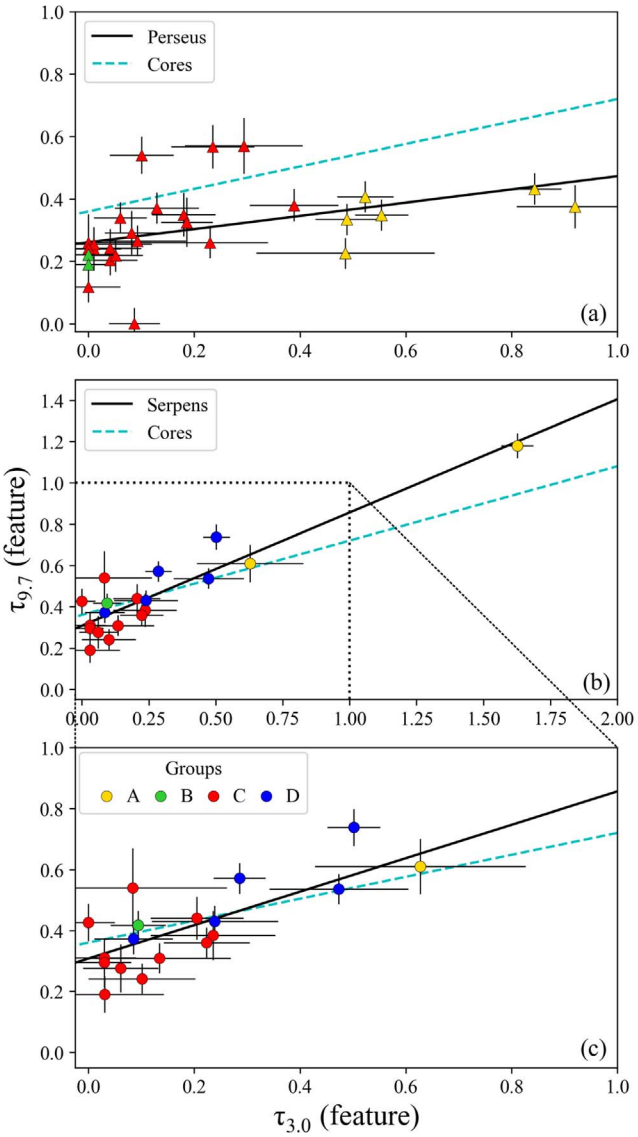

Figure 6. Water ice and silicate band optical depth correlations for Perseus (a) and Serpens ((b) and (c)) targets. The error bars are of 3σ significance. The solid black line is a least-squares fit to all targets in the cloud. The dashed blue line is the correlation derived from dense cores in Boogert et al. (2011). The colors of the data points correspond to the groupings defined in Section 5.1 and Figure 4. Panel (c) zooms in on the lower-extinction Serpens targets.

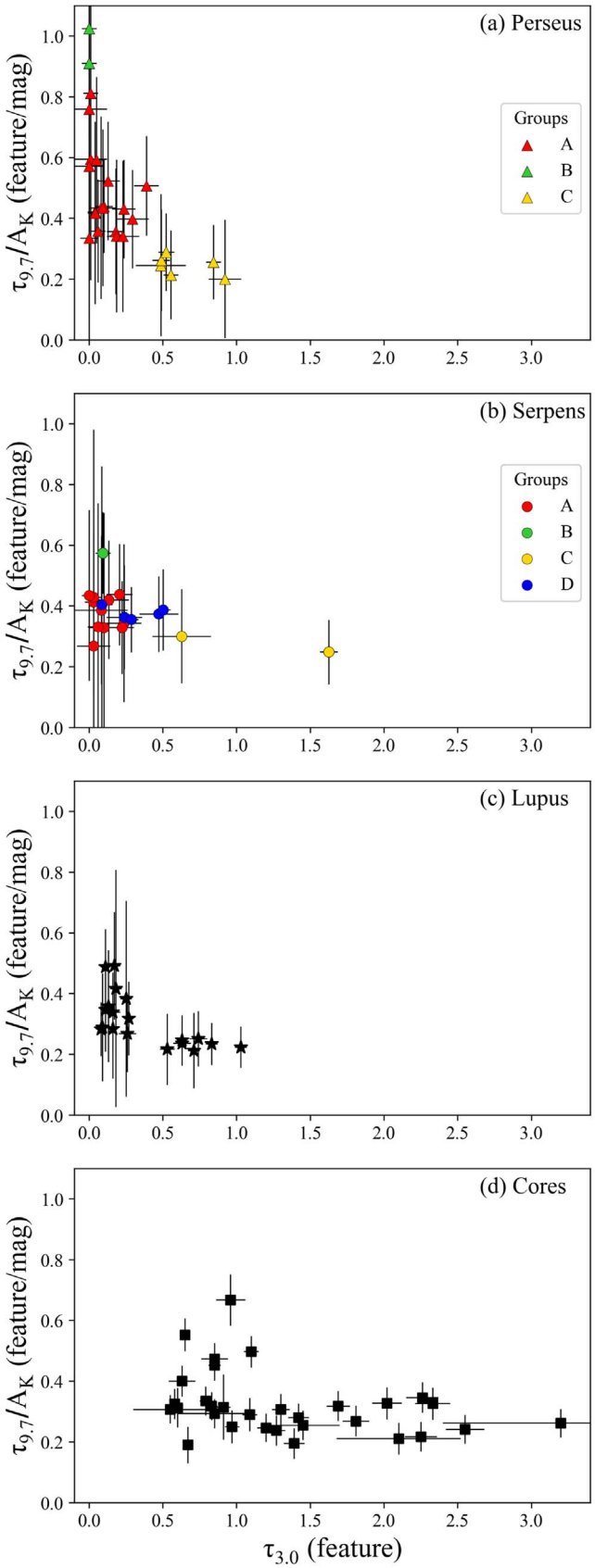

Figure 7. Relation between the $\tau_{9.7}/A_K$ ratio and $\tau_{3.0}$ for Perseus (a), Serpens (b), and Lupus (c) clouds, as well as isolated dense cores (d). The error bars are of 3σ significance. The colors of the data points in panels (a) and (b) correspond to the groupings in Figure 4.

is only detected in Ser-7. Despite the good S/N of the spectra for the other two ice targets, Per-6 and Per-11, there is no significant detection of CH_3OH (Figure 9). This also shows that the 6.85 μm absorption feature, which is detected in all three targets, is for at most a small fraction due to the C–H deformation mode of CH_3OH. The most promising candidate is solid NH_4^+ (Raunier et al. 2003; Schutte & Khanna 2003; Gibb et al. 2004; Boogert et al. 2008). For other potential contributors, we refer to Keane et al. (2001).

The CH_3OH ice column density is calculated using an integrated band strength of $A = 1.6 \times 10^{-17}$ cm molecule^{-1} (Kerkhof et al. 1999). This A-value is an average across different mixtures with a variation of $\sim$20%. The abundance relative to H_2O is $21 \pm 2\%$ for Ser-7 (Table 5). The uncertainty reflects baseline fluctuations, and does not take into account the

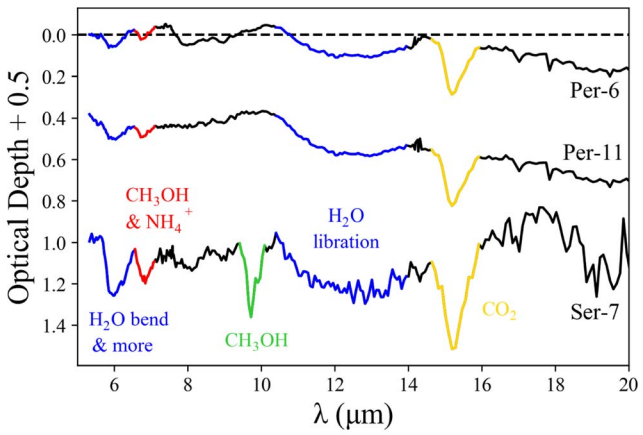

Figure 8. 5–20 μm optical depth spectra of the targets with the strongest ice absorption features: Per-6, Per-11, and Ser-7, from top to bottom, respectively. A model for the 9.7 μm and 18 μm silicate bands has been subtracted. Ice absorption feature identifications are indicated. The 6 and 6.85 μm absorption features consist of overlapping ice bands, and not all components have been securely identified. The structure between 8–9 μm toward Per-6 is likely due to insufficiently corrected photospheric absorption. Offsets of 0.5 along the y-axis are applied for clarity.

Table 5
CH_3OH Ice Abundances

Alias	A_K mag	$N(H_2O)$ (10^{17} cm^{-2})	$N(CH_3OH)$ (10^{17} cm^{-2})	$\frac{N(CH_3OH)}{N(H_2O)}$
Ser-7	4.75 ± 0.44	26.33 ± 0.97	5.4 ± 0.5	0.21 ± 0.02
Per-6	0.75 ± 0.07	6.29 ± 1.36	<0.64	<0.10
Per-11	1.69 ± 0.07	13.66 ± 0.82	<0.39	<0.03

Note. The three targets with deep ice bands, as in Figure 8, including their aliases, extinctions, water ice column densities, methanol column densities, and their methanol to water ice ratios.

uncertainty in the A-value. Ser-7 has the highest CH_3OH abundance measured toward a background star of a dense cloud or core to date (Boogert et al. 2011; Chu et al. 2020). It is also significantly higher (factors of 2–6) than the upper limits derived for the other two ice targets (Table 5).

5.6. Spatial Context

In order to put the variations in the dust and ice properties observed toward the Perseus and Serpens background stars in a spatial context, we compare them to infrared images, extinction maps, and the young stellar object (YSO) population.

We use Spitzer extinction maps and infrared images that were produced by the c2d Legacy project (Evans et al. 2003, 2009). The Perseus extinction map, derived from near-infrared colors, has a resolution of 180″ and has a minimum of $A_V = 2$ mag. For Serpens, the resolution is 90″ and starts at the $A_V = 5$ mag cloud boundary. For the infrared images, we chose the IRAC1 filter at 3.6 μm, as this is more sensitive to dust scattering than the longer wavelengths. To select the protostellar population, we used the Spitzer c2d catalogs (Evans et al. 2009) available through the InfraRed Sky Archive (IRSA) interface. All Perseus and Serpens targets with infrared spectral indices $\alpha > -0.3$ were selected, where α follows the definition of Lada (1987). These represent the most embedded population of stars. We then designated targets with $-0.3 \leqslant \alpha < 0.3$ as "flat spectrum" YSOs, and targets with $\alpha \geqslant 0.3$ as Class I targets. We also added the more embedded Class 0 sources, which are harder to identify using Spitzer photometry alone due to their weakness. Thirteen Class 0 targets in Perseus were obtained from Jørgensen et al. (2006), and four in Serpens from Hogerheijde et al. (1999). The YSO populations and the background star groups defined by the $\tau_{9.7}$ versus A_K correlation (Section 5.1) are indicated on the IRAC images and extinction maps in Figures 10 and 11 for Perseus and Serpens, respectively.

For Perseus, the majority of the Group A ("dense" cloud-type) targets are located in the western portion of the cloud (Figure 10). This is also where the five Class 0 YSOs are all located. Class 0 envelopes extend to typically 1″ in Perseus (Enoch et al. 2006). Group A target Per-9 is located 143″ (35,631 au) from the Class I YSO IRAS 03271+3013. Another Group A target, Per-12, is located 67″ (16,819 au) from the Class 0 YSO IRAS 03292+3039. The smallest distance is 53″ between the background star Per-11 and the Class 0 target [DCE2008] 081, and therefore it appears that none of the background stars significantly traces Class 0 envelopes.

It is noteworthy that the two Group B ("diffuse ISM-like") targets are located in the western part of Perseus as well. They are located at the edges of extinction enhancements, and somewhat further away from YSOs compared to several Group A targets. The number of targets is small, however, and these trends are not statistically significant. The median distance between the six Group A targets and nearest YSOs is 176″ with a standard deviation of 240″; the distances of the two Group B targets and their nearest YSOs are 657″ and 671″.

The Perseus targets with the deepest ice bands, Per-6 (Group C) and Per-11 (Group A), are also located in the western region of Perseus. Per-11 is located among a small cluster of Class I and "flat spectrum" YSOs, but Per-6 is also located near such YSOs. Overall, these results indicate a significant variety of dust properties within Perseus. Dense-cloud-like dust is found within the vicinity (~15,000 au) of YSOs but also in regions without YSOs. Diffuse ISM-like dust may have strong ice absorption, and is also found in the denser regions.

In Serpens, most of the Class I and "flat spectrum" YSOs are concentrated in two clusters, one located in the upper half of Serpens, and the other, "Ser/G3-G6," located around the middle of the molecular cloud (Zhang et al. 1988). The four Class 0 YSOs are toward the center of the upper cluster (Figure 11). The Group A target Ser-7 is located at the edge of Ser/G3-G6, but within an arcminute of the YSO cluster. Ser-7 has very deep ice bands, and a very large CH_3OH ice abundance. This likely reflects a high density associated with the star formation in this cluster. The single Group B target is located in a local extinction minimum. Group D targets (intermediate between "diffuse ISM-like" and "dense-like" dust) are spread out along the molecular cloud, in some cases located near the edges of local cores or near YSOs, but certainly not in all cases.

Overall, as for Perseus, no clear correlations stand out for Serpens, and the dust properties are governed by local physical conditions not evident in these tracers. The distances between the two Group A targets and their nearest YSOs are 180″ (standard deviation 23″); for the one Group B target, there is a distance of 285″; for the six Group D targets, there is a median distance of 118″ with a standard deviation of 105″.

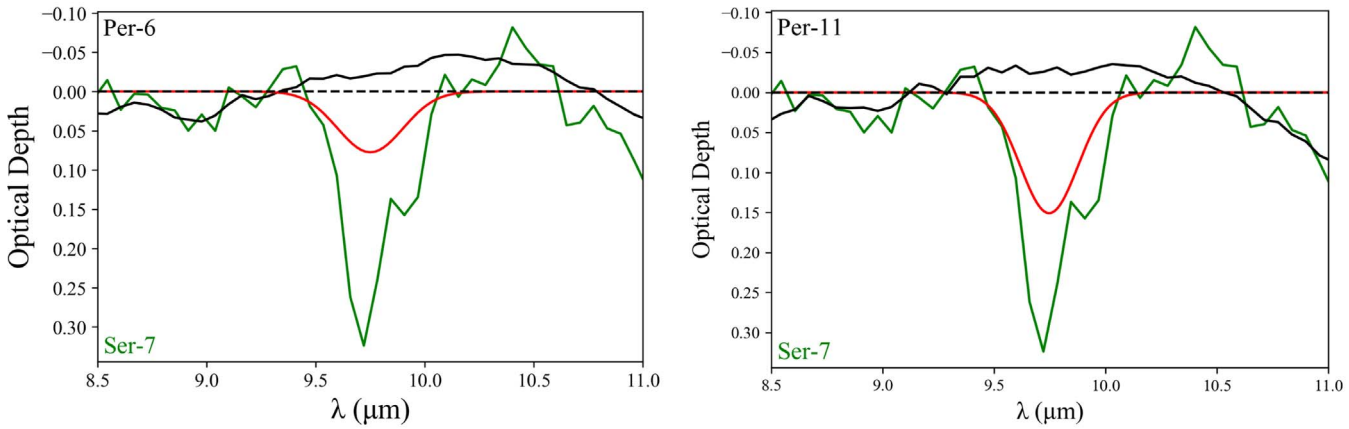

Figure 9. Comparison of the deep CH_3OH feature in Ser-7 (green) to a selection of other targets with deep 3.0 μm H_2O ice bands, Per-6 (left) and Per-11 (right) in black. A model for the 9.7 μm silicate feature has been subtracted. Ser-7 has an extinction of $A_K = 4.75 \pm 0.44$, Per-6 of $A_K = 0.75 \pm 0.07$, and Per-11 of $A_K = 1.69 \pm 0.07$. Gaussians (red) demonstrate the expected peak depths if the CH_3OH abundance relative to H_2O were the same in these targets as in Ser-7. CH_3OH is clearly absent, and upper limits are listed in Table 5.

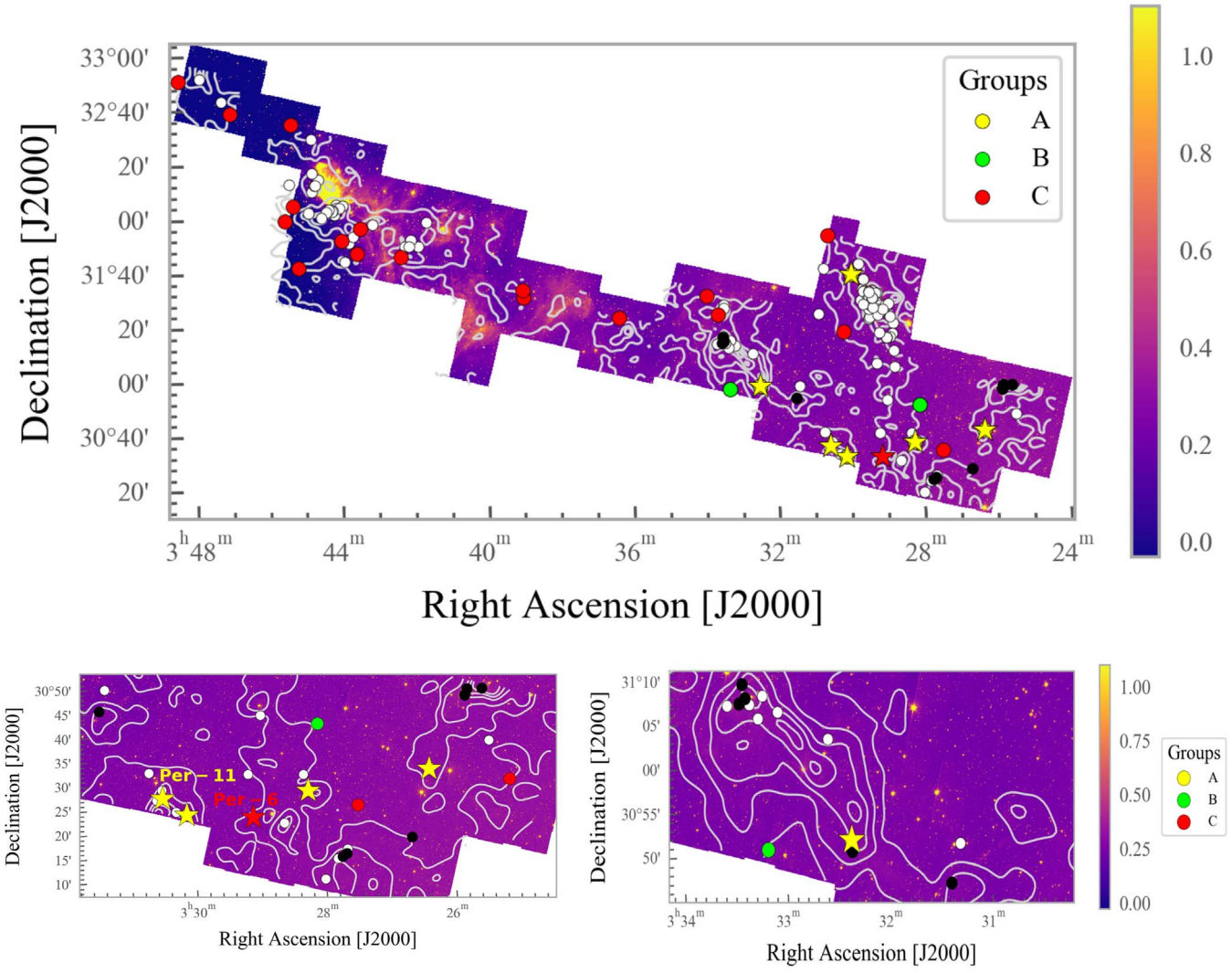

Figure 10. Top panel: location of the background stars (yellow, green, and red circles and star symbols, as defined in Figure 4) compared to Class 0 (black) and Class I and "flat spectrum" (white) young stellar objects (YSOs) observed toward Perseus overlaid the IRAC1 map (3.6 μm). The colorbar is in units of MJy sr^{-1}. The contours represent the extinction map of A_V levels of 3, 6, 12, 18, and 24 mag. The star symbols represent the targets that exhibit strong ice features, at $\tau_{3.0} > 0.5$ within the uncertainties. Bottom panels: zoomed-in regions of the top panel, The red star symbol in the left panel represents Per-6, and the yellow star symbol to the far left Per-11, both of which have particularly deep ice absorption bands.

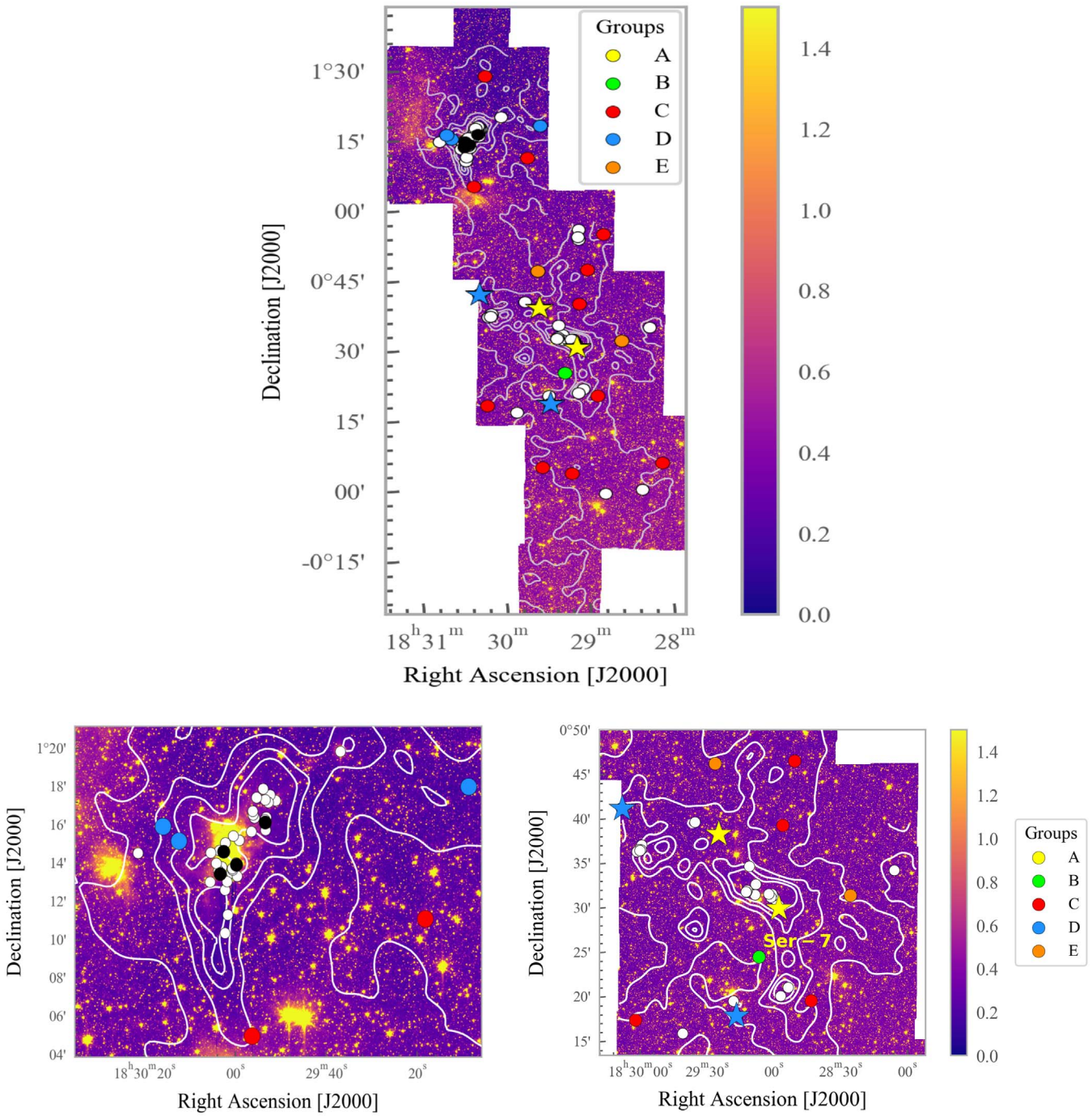

Figure 11. Top panel: location of the background stars (colored bullets and star symbols, as defined in Figure 4) compared to Class 0 (black) and Class I and "flat spectrum" (white) YSOs observed toward Serpens overlaid the IRAC1 map (3.6 μm). The colorbar is in units of MJy sr^{-1}. The contours represent the extinction map of A_V levels of 3, 6, 12, 18, and 24 mag. The star symbols represent the targets that exhibit strong ice features, at $\tau_{3.0} > 0.5$ within the uncertainties. Bottom panels: zoomed-in regions for known clusters in Serpens, the "core" (left) and "Ser/G3-G6" (right). The yellow asterisk near the center represents Ser-7, which exhibits particularly strong ice features.

6. Discussion

6.1. The $A_K/\tau_{9.7}$ Ratio in Grain Growth Models

Grain growth, starting when most grains are much smaller than the near-infrared wavelength, i.e., in the Rayleigh limit, will increase A_K initially. But when the grain sizes become comparable to or larger than $\sim$0.4 μm ($\lambda/2\pi$), gray extinction becomes important, and A_K (per dust mass), derived from the near-infrared color excess, will decrease. This implies that the observed $A_K/\tau_{9.7}$ reduction in dense clouds (Figure 4) could trace a moderate amount of grain growth. This is also concluded by Ormel et al. (2011) based on grain growth models. These models further infer that the grain growth is in the form of aggregates of ice-coated silicate and ice-coated carbonaceous grains. The increased stickiness of ice-coated grains is key in the coagulation process. The observed relation between $A_K/\tau_{9.7}$ and the ices ($\tau_{3.0}$) will be discussed in Section 6.2.

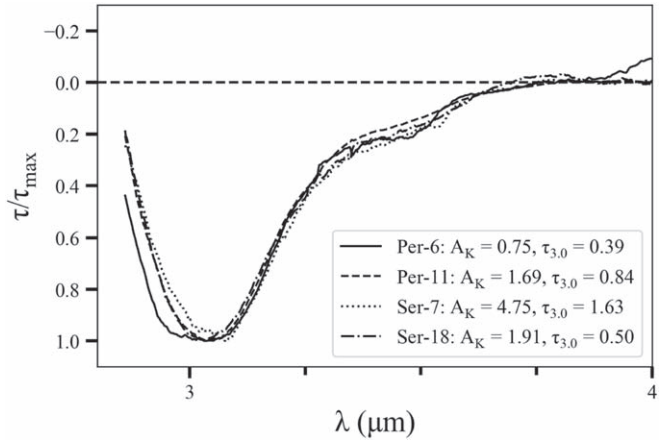

Figure 12. Profile of the 3 μm water ice bands observed toward four targets tracing a range of extinctions ($A_K = 0.75$–4.75). Per-6 is Group C, Per-11 is Group A, Ser-7 is Group A, and Ser-18 is Group D. The spectra have been normalized and smoothed to a resolving power of 100. Little variation is evident in the long-wavelength wing, indicating insignificant growth of the relative population of grains larger than ∼0.5.

Such moderate grain growth is consistent with the invariant profiles of the 9.7 μm absorption bands. This was also the primary conclusion of the extensive study by Van Breemen et al. (2011). The coagulated grains are too small to affect the profile of the 3.0 μm ice band as well, as little variation is observed as a function of extinction (Figure 12). The long-wavelength wing, which is thought to be affected by large-grain scattering, limits the grains to sizes of $\frac{3}{2\pi} \approx 0.5$ μm and less. Some variation is observed on the short-wavelength wing, which might be a result of NH_3 abundance variations due to the N–H stretching mode at 2.9 μm. Indeed, the target with the strongest short-wavelength wing also shows a more pronounced 3.47 μm feature, which results from ammonia hydrates (Dartois & d'Hendecourt 2001).

A different scenario was discussed in Chiar et al. (2007) and Ormel et al. (2011). Considering that the *K*-band extinction is primarily caused by carbonaceous grains, the reduction of the $\tau_{9.7}/A_K$ ratio (Figure 4) is possible if growth is limited to silicate grains in the inner cloud regions. These grains would need to be much larger than 1 μm so that they do not contribute to the $\tau_{9.7}$ absorption feature (and also not to A_K), and not change its profile. In the models of Ormel et al. (2011), the silicate absorption feature disappears for timescales longer than 1 Myr at a density of 10^5 cm^{-3}, or at shorter timescales at higher densities. Thus, in this scenario, large ice-rich silicate grains reside in the inner, dense regions of the clouds, while the small silicate grains in the outer regions are responsible for the 9.7 μm absorption feature. Carbonaceous grains would not form such large grains, perhaps due to not acquiring ice mantles. It is unclear why this would be the case. In fact, the increase of $\tau_{3.0}$ as a function of A_K, as observed in both Perseus and Serpens (Figure 5), is difficult to explain with ice-less carbonaceous grains. If only silicate grains, tracing the outer cloud layers, are covered with ice mantles, the $\tau_{3.0}$ as a function of A_K would flatten, which is clearly not the case. Thus, overall, this scenario seems less likely.

6.2. $A_K/\tau_{9.7}$ Variations and Relations with Ices and Dense Core Formation

Striking variations in the relation between A_K and $\tau_{9.7}$ are observed (Figure 4). At the highest extinctions, the targets are

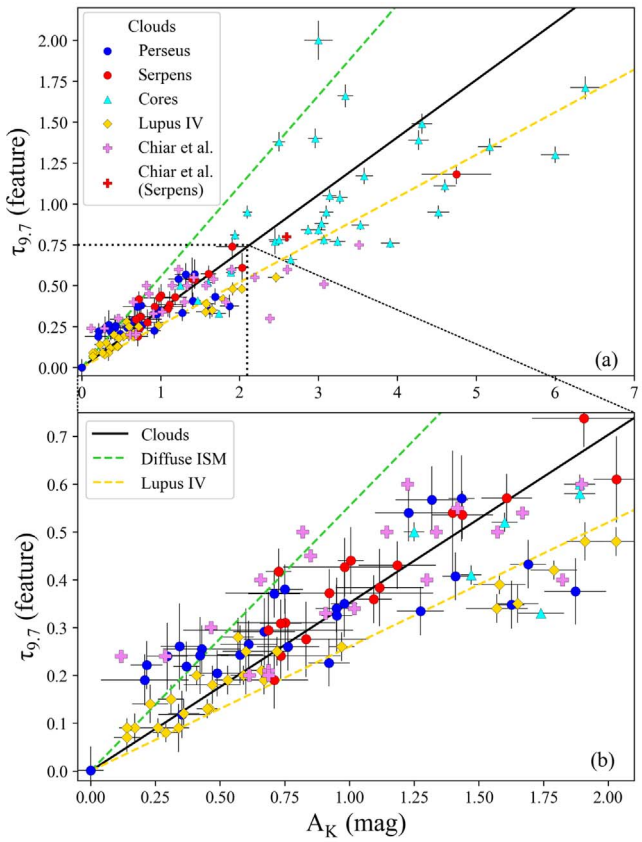

Figure 13. Silicate ice and extinction correlation for the Perseus, Serpens, Lupus, Taurus, and Chameleon I molecular clouds, as well as several dense cores, taken from Chiar et al. (2007), and Boogert et al. (2011, 2013). The bottom panel zooms in on the lower extinctions. The data points are color-coordinated by cloud, as indicated. The black line is the linear fit to all targets. The green dotted line is the diffuse ISM correlation (Whittet 2003), and the yellow dotted line is the Lupus IV correlation (Boogert et al. 2011). The error bars, when available, are 3σ. Four Lupus IV sources have upper limits that are consistent with the general correlation but are not included in this graph. The isolated dense core targets near the diffuse ISM relation trace L328, which is thought to be strongly contaminated by foreground dust absorption.

trending to lie systematically below the linear fit, i.e., $\tau_{9.7}$ is suppressed relative to A_K. For Perseus, this inflection occurs at $A_K \sim 1.2$ ($A_V \sim 10$, assuming $A_V/A_K = 8.4$), while for Serpens, it is near $A_K \sim 2$ ($A_V \sim 17$). Below this inflection point, the data points are located between the diffuse and dense cloud relations. Above this inflection point, the data points tend to follow the dense cloud relation. The same is observed for the third cloud in our survey, Lupus, which shows an inflection point similar to Perseus (Boogert et al. 2013).

In Figure 13, we accumulate all $\tau_{9.7}$ and A_K data of other clouds and cores known to us (Chiar et al. 2007; Boogert et al. 2011, 2013). In addition to Perseus, Serpens, and Lupus (I and IV), this includes targets tracing Taurus, IC 5146, Barnard 68, Chameleon I, and a range of isolated dense cores. The isolated dense cores extend the A_K range to much higher values. An overall correlation is visible, but the scatter is large. The fitted line to all the data lies between the diffuse ISM and dense core correlations, just as for our individual cloud fits. An overall inflection point, after which the targets center around the dense cloud correlation, is also visible, near $A_K \sim 1.5$ ($A_V \sim 13$). Thus, overall, assuming that the $\tau_{9.7}/A_K$ ratio is a measure of grain sizes (Section 6.1), Figure 13 shows that the dust

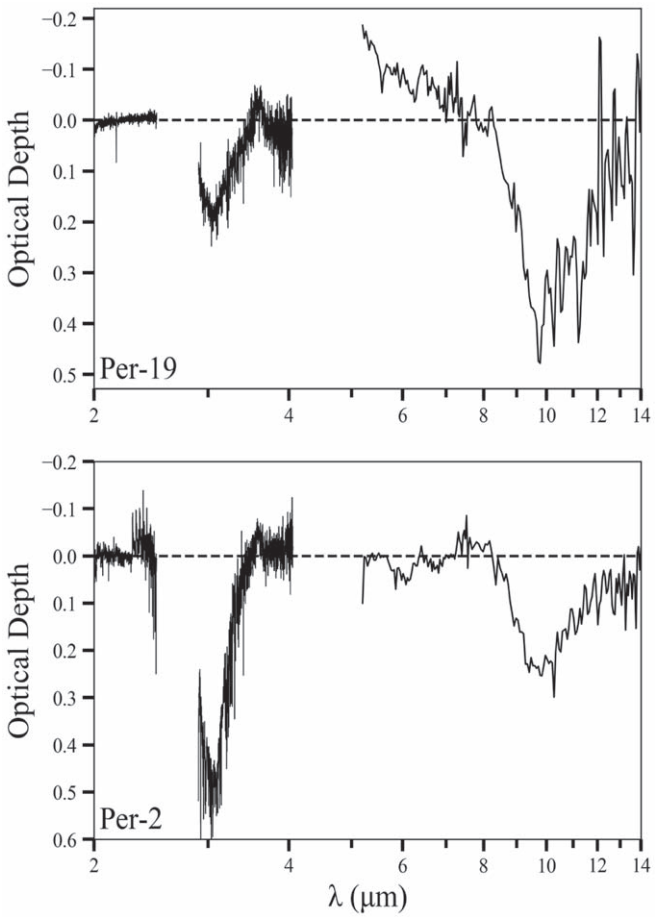

Figure 14. Comparison of the 3.0 and 9.7 μm ice and silicate bands of the targets Per-19 and Per-2. Both targets have similar A_K values, but Per-19 has a much deeper 9.7 μm silicate band (and thus belongs to "diffuse ISM" Group B). Conforming with its diffuse ISM nature, Per-19 has a factor of ~2.5 less water ice than Per-2, as seen by the shallower 3.0 μm H_2O feature. Such variations might point to a relation between ice formation and grain coagulation. The negative optical depth values between 5–8 μm for Per-19 are due to the choice of a local baseline for the 9.7 μm absorption feature, as noted in Table 3.

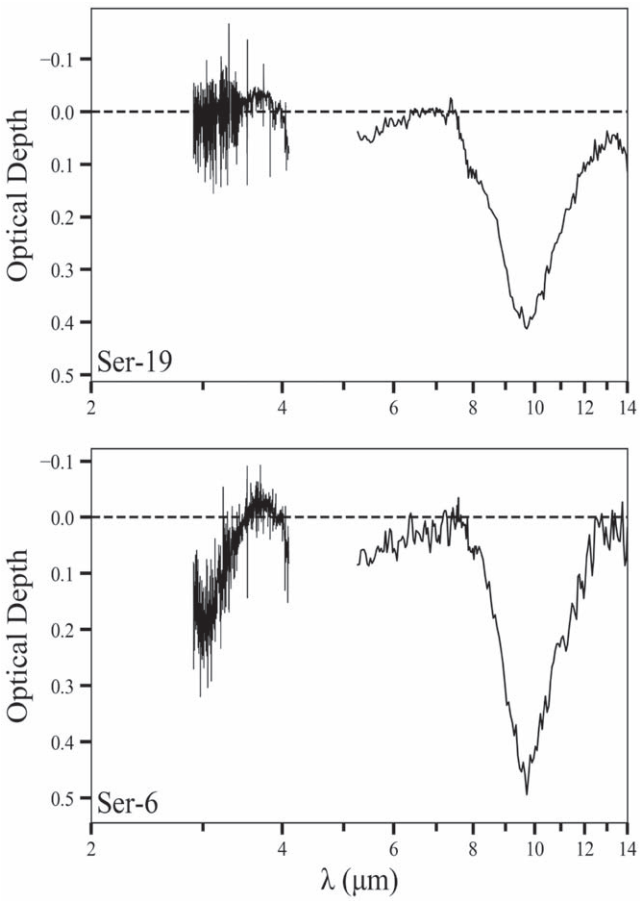

Figure 15. Targets Ser-19 and Ser-6 have similar A_K values and 9.7 μm silicate band depths, but only Ser-6 displays the 3.0 μm H_2O feature. The *L*-band portions have been smoothed to a resolving power of 25. This comparison indicates that ice formation is not the only factor that affects coagulation as traced by the $A_K/\tau_{9.7}$ ratio.

coagulation process follows a smilar pattern across different clouds.

It does appear that these $\tau_{9.7}/A_K$ variations relate to the ice band optical depths. For Perseus, the $\tau_{3.0}$ values for Group A targets (lowest $\tau_{9.7}/A_K$) are significantly higher compared to all other targets, even those at similar A_K (Figure 5). Indeed, the Group A targets are well separated in the $\tau_{9.7}/A_K$ versus $\tau_{3.0}$ correlation plots (Figure 7). The Lupus Cloud shows a similar behavior. For Serpens, targets with the largest $\tau_{9.7}/A_K$ ratios, have the largest $\tau_{3.0}$ values, although very few lines of sight with deep 3.0 μm ice bands are available.

The threshold for ice formation is similarly low for all clouds ($A_V \sim 2.6$–3.4; Section 6.3), and thus it appears that not only the mere presence of ice on the grains, but also the ice column density (traced by $\tau_{3.0}$), is an important factor in the grain growth process. This, in turn, relates to the cloud density, as lines of sight with deeper ice bands likely trace higher densities deeper into the cloud.

Indeed, for both scenarios discussed in Section 6.1, the $\tau_{9.7}$ versus A_K relation is a measure of the density structure of the clouds. The inflection point in this relation reflects a transition to higher-density inner cloud regions where grain growth accelerates. This implies that the density structure for Serpens is shallower than for Perseus, Lupus, and other dense cores, although the density at the cloud edge is similar for all these clouds, as evidenced by their similar ice formation thresholds (Section 6.3). Within Perseus, however, coagulation is strongest for the targets with the largest ice column densities.

In addition to the overall trends described above, there are deviations, indicating that local conditions, such as density fluctuations across the cloud also matter. Such local scatter in the $\tau_{9.7}$ versus A_K plots was also noted for Lupus (Boogert et al. 2013). Figure 14 compares the optical depth spectra of Per-19 (Group C) and Per-2 (Group A), which have similar A_K values, but Per-19 has a 50% deeper 9.7 μm silicate band. Conforming with its diffuse ISM nature, Per-19 has a factor of ~2.5 less water ice than Per-2. Thus, Per-19 appears to trace lower-density cloud material. In contrast, Ser-19 and Ser-6 have similar $\tau_{9.7}$ and A_K at very different $\tau_{3.0}$ (Figure 15). Ser-19 is in fact the only Serpens target without ice. It is relatively isolated on the edge of the cloud, but it is unclear if this plays a role. Unfortunately, Ser-19 and Ser-6 have uncertainn $\tau_{9.7}/A_K$ ratios (Group C), precluding a distinction between dense-like (Group A) or diffuse-like (Group B) dust.

It is worthwhile to note that the inflection points in the A_K versus $\tau_{9.7}$ relation of $A_V \sim 10$ and $A_V \sim 17$ for Perseus and Serpens, respectively, are comparable to the dense core formation thresholds in these clouds. Enoch et al. (2007)

derive dense core formation thresholds of $A_V \sim 8$ and $A_V \sim 15$ from comprehensive infrared and submillimeter surveys. This reinforces the idea that the dust coagulation process is enhanced at higher densities.

6.3. Ice Formation Threshold

The relation between A_K and $\tau_{3.0}$ (Section 5.2, Figure 5) for Serpens shows a cut-off along the A_K axis of 0.616 ± 0.087 ($A_V = 5.17 \pm 0.06$), which is approximately twice that of Perseus ($A_V = 2.65 \pm 0.25$), Lupus IV ($A_V = 2.10 \pm 0.59$; Boogert et al. 2011), and Taurus ($A_V = 3.2 \pm 0.1$; Whittet et al. 2001). This might be attributed to extinction by unrelated foreground dust. Serpens is located at a larger distance (420 ± 15 pc) than all these other clouds: 294 ± 15 pc for Perseus, 141 ± 7 pc for Taurus, and 189 ± 13 pc for Lupus (Ortiz-León et al. 2018; Zucker et al. 2019). To the first order, the foreground extinction due to diffuse dust in the Galactic plane may be estimated by scaling to the extinction of $A_V \sim 30$ toward the Galactic center (Rieke et al. 1989 and references therein) at ~8 kpc. This results in foreground contributions of $A_V \sim 1.6$, 1.1, 0.7, and 0.5 mag for Serpens, Perseus, Lupus IV, and Taurus, respectively. Models using Gaia-derived distances (Zucker et al. 2019), however, point to a larger foreground contribution ($A_V = 3.0$) for Serpens than for all the other clouds ($A_V = 1.0$). This could be related to its location closer to the Galactic plane ($b \sim +4°$), more directed to the Galactic center ($l \sim 30°$) than the other clouds.

Overall, when correcting for the larger foreground extinction toward Serpens, it thus seems that H_2O ice is formed at similar depths for all studied clouds. This would be at $A_V \sim 2.6$–3.4, or ~1.6–2.4 when subtracting the 1.0 mag foreground for all (Zucker et al. 2019). If we further correct for the fact that the observations trace both the front and back of the clouds, the cloud depth at which H_2O ice is abundantly formed is $A_{Vf} \sim 0.8$–1.2 mag. Following Hollenbach et al. (2009), this could indicate that the cloud edges have similar densities (n), provided that they experience similar interstellar radiation fields $F_0 G_0$:

$$A_{Vf} = 0.56 \times \ln\left(\frac{G_0 F_0 Y}{n(O)\nu_0}\right) \quad (6)$$

where Y is the total yield of photodesorbing H_2O ice, and ν_O is the vibrational frequency of O atoms bound to a grain surface related to dust temperature. For typical conditions (Hollenbach et al. 2009), this corresponds to $n \sim 3 \times 10^4$ at $A_{Vf} \sim 0.8$–1.2 mag.

A higher threshold was observed toward the Ophiuchus Cloud (Tanaka et al. 1990) and is usually ascribed to the presence of a nearby O- and B-stars, increasing F_0, photodesorbing the ices. No such sources for a high ultraviolet radiation field near the other clouds are known. Note that if the larger cut-off in the relation between A_K and $\tau_{3.0}$ is not caused by foreground dust, Equation (6) would imply a lower Serpens cloud edge density compared to the other clouds by a factor of ~7.

6.4. CH_3OH

One of our targets, Ser-7, shows a very high CH_3OH abundance of ~21% relative to H_2O, surpassing previous records for background stars of L694 (~14%; Chu et al. 2020) and L429-C (~12%; Boogert et al. 2011). This target was also noted as containing high abundances of other organic molecules, such as methane (CH_4) and, tentatively, solid acetylene (C_2H_2) at 13.5 μm (Knez et al. 2008, 2012).

The CH_3OH abundance toward Ser-7 is significantly larger than the upper limits derived for other Serpens and Perseus background stars (Figure 9). It approaches the largest CH_3OH ice abundances observed toward YSOs in Serpens (28%; Pontoppidan et al. 2004; Perotti et al. 2020). Of all background stars in our sample, Ser-7 is closest to a YSO (2MASSJ18285277+0028463), which is a member of the Ser/G3-G6 cluster of Class I and "flat spectrum" YSOs. At an angular distance of 23″ (5725 au), the large CH_3OH abundance might trace the very outer edges of the envelope of this flat spectrum YSO, or the high-density core material within which the cluster formed. While CH_3OH is also expected to form at low densities (e.g., Qasim et al. 2018), its formation is strongly enhanced at high densities (10^5 cm^{-3}) when CO rapidly freezes out (Cuppen et al. 2009). Indeed, so far all CH_3OH ice detections toward background stars trace sight-lines with very high extinction, above a threshold of $A_V \sim 18$ ($A_K \sim 2$; Boogert et al. 2015; Chu et al. 2020). Ser-7 is the only target in our Serpens and Perseus sample with an extinction ($A_K = 4.75 \pm 0.44$) above this threshold.

7. Summary and Future Work

We present 2–4 and 5–20 μm spectra of a sample of 28 stars behind the Perseus and 21 stars behind the Serpens molecular clouds. We fitted the target spectra using a combination of template spectra from the IRTF spectral database and photospheric model spectra, combined with extinction curves, laboratory H_2O ice spectra, and silicate absorption spectra to derive A_K, $\tau_{3.0}$, and $\tau_{9.7}$ values. Correlation plots of $\tau_{9.7}$ versus A_K show a variation of a factor of ~2 for both clouds. Combining our $\tau_{9.7}$ and A_K values with those available in the literature indicates that such scatter is common.

In general, the $\tau_{9.7}/A_K$ ratios are reduced relative to the diffuse ISM. The largest reductions, up to a factor of 2, are visible above $A_K \sim 1.2$ for Perseus and Lupus, and above $A_K \sim 2.0$ for Serpens. A picture emerges that grains, after acquiring ice mantles (at $A_K \sim 0.2$–0.4), grow to moderate sizes due to higher densities deeper in the cloud, especially above $A_K \sim 1.2$–2. A significant population of grains larger than ~0.5 μm is unlikely, however, as this would increase the $\tau_{9.7}/A_K$ ratio, and would also change the profiles of the 3.0 and 9.7 μm absorption profiles, which is not observed.

The regions with the lowest $\tau_{9.7}/A_K$ ratios are also the regions where dense core (and thus star) formation will take place, considering similar dense core formation extinction thresholds. Indeed, Serpens stands out by having a factor of ~2 higher inflection in the $\tau_{9.7}$ versus A_K relation, and also a factor of 2 larger dense core formation threshold. These aspects may indicate that Serpens has an overall shallower density profile than the other clouds.

We derived H_2O ice formation thresholds of $A_V \sim 2.6$–3.4 for all studied clouds, after correction for a 2 mag larger foreground extinction toward Serpens. This threshold is well below the extinctions where the lowest $\tau_{9.7}/A_K$ ratios are observed. Thus we conclude that, in agreement with the grain growth models by Ormel et al. (2011), grain coagulation is facilitated by ice mantles, and enhanced at higher densities. Targets tracing the highest ice column densities (proportional to $\tau_{3.0}$), and thus likely densities, have the lowest $\tau_{9.7}/A_K$ ratios.

Besides the overall trends, we also found a large scatter in the $\tau_{9.7}/A_K$ ratio across small A_K intervals. Using extinction maps, infrared images, YSO and molecular outflow locations, we did not find strong correlations of these variations with cloud location. Finally, we found three targets (Per-6, Per-11, Ser-7) with particularly deep ice bands, of which Ser-7 has an especially high CH_3OH ice abundance of 21% relative to H_2O. This is significantly higher than the upper limits in the other sources, which is attributed to high densities in a local star formation region.

A larger sample of sight-lines, fully covering a wide range of A_K values and molecular cloud conditions, is needed to further constrain the relation between ice formation, the silicate band, and continuum extinction. A confirmation of the inflection in the A_K versus $\tau_{9.7}$ relation is needed, as well as studies of the origin of the scatter in the $\tau_{9.7}/A_K$ ratio, in particular the relation with local density. Future work will rely heavily on observations with the James Webb Space Telescope, enabling the construction of detailed maps of A_K, $\tau_{3.0}$, and $\tau_{9.7}$, facilitating an assessment of the relation between grain coagulation and other cloud properties.

We thank Lee Mundy and Ewine van Dishoeck for their help with the early stages of this project. We thank Megan Kiminki who worked on this project while an REU student at the SETI Institute, supported by NSF grant AST-1359346. M.C.L.M. thanks the Institute for Astronomy at UH Manoa for their hospitalty, and Columbia University in the City of New York and the I.I. Rabi Scholars Program for their generous financial support. We thank the referee for insightful comments, in particular on the cloud distances and foreground extinction correction, that helped improve this paper. This work is based on observations made at the IRTF and Keck telescopes. We wish to extend our special thanks to those of Hawaiian ancestry on whose sacred mountain of Maunakea we are privileged to be guests. The observations presented herein would not have been possible without their generosity. The authors recognize that the summit of Maunakea has always held a very significant cultural role for the indigenous Hawaiian community. We are thankful to have the opportunity to use observations from this mountain.

ORCID iDs

M. C. L. Madden https://orcid.org/0000-0002-0913-6110
A. C. A. Boogert https://orcid.org/0000-0001-9344-0096
J. E. Chiar https://orcid.org/0000-0003-2029-1549
Y. J. Pendleton https://orcid.org/0000-0001-8102-2903
A. G. G. M. Tielens https://orcid.org/0000-0003-0306-0028

References

Boogert, A. C. A., Chiar, J. E., Knez, C., et al. 2013, ApJ, 777, 73
Boogert, A. C. A., Gerakines, P. A., & Whittet, D. C. B. 2015, ARA&A, 53, 541
Boogert, A. C. A., Pontoppidan, K. M., Knez, C., et al. 2008, ApJ, 678, 985
Boogert, A. C. A., Huard, T. L., Cook, A. M., et al. 2011, ApJ, 729, 92
Cambrésy, L., Rho, J., Marshall, D. J., & Reach, W. T. 2011, A&A, 527, A141
Chiar, J. E., Adamson, A. J., & Whittet, D. C. B. 1996, ApJ, 472, 665
Chiar, J. E., Ennico, K., Pendleton, Y. J., et al. 2007, ApJL, 666, L73
Chu, L. E. U., Hodapp, K., & Boogert, A. 2020, ApJ, 904, 86
Cuppen, H. M., van Dishoeck, E. F., Herbst, E., & Tielens, A. G. G. M. 2009, A&A, 508, 275
Cushing, M. C., Vacca, W. D., & Rayner, J. T. 2004, PASP, 116, 362
Dartois, E., & d'Hendecourt, L. 2001, A&A, 365, 144
Decin, L., Morris, P. W., Appleton, P. N., et al. 2004, ApJS, 154, 408
Enoch, M. L., Glenn, J., Evans, N. J. I., et al. 2007, ApJ, 666, 982
Enoch, M. L., Young, K. E., Glenn, J., et al. 2006, ApJ, 638, 293
Evans, N. J. I., Allen, L. E., Blake, G. A., et al. 2003, PASP, 115, 965
Evans, N. J. I., Dunham, M. M., Jørgensen, J. K., et al. 2009, ApJS, 181, 321
Gibb, E. L., Whittet, D. C. B., Boogert, A. C. A., & Tielens, A. G. G. M. 2004, ApJS, 151, 35
Harvey, P. M., Chapman, N., Lai, S.-P., et al. 2006, ApJ, 644, 307
Hogerheijde, M. R., van Dishoeck, E. F., Salverda, J. M., & Blake, G. A. 1999, ApJ, 513, 350
Hollenbach, D., Kaufman, M. J., Bergin, E. A., & Melnick, G. J. 2009, ApJ, 690, 1497
Hudgins, D. M., Sandford, S. A., Allamandola, L. J., & Tielens, A. G. G. M. 1993, ApJS, 86, 713
Indebetouw, R., Mathis, J. S., Babler, B. L., et al. 2005, ApJ, 619, 931
Jørgensen, J. K., Harvey, P. M., Evans, N. J. I., et al. 2006, ApJ, 645, 1246
Keane, J. V., Tielens, A. G. G. M., Boogert, A. C. A., Schutte, W. A., & Whittet, D. C. B. 2001, A&A, 376, 254
Kerkhof, O., Schutte, W. A., & Ehrenfreund, P. 1999, A&A, 346, 990
Knez, C., Moore, M. H., Ferrante, R. F., & Hudson, R. L. 2012, ApJ, 748, 95
Knez, C., Moore, M., Travis, S., et al. 2008, in IAU Symp. 251, Organic Matter in Space, ed. S. Kwok & S. Sanford (Cambridge: Cambridge Univ. Press), 47
Lada, C. J. 1987, in IAU Symp. 115, ed. M. Peimbert & J. Jugaku (Cambridge: Cambridge Univ. Press), 1
McClure, M. 2009, ApJL, 693, L81
McLean, I. S., Becklin, E. E., Bendiksen, O., et al. 1998, Proc. SPIE, 3354, 566
Ormel, C. W., Min, M., Tielens, A. G. G. M., Dominik, C., & Paszun, D. 2011, A&A, 532, A43
Ortiz-León, G. N., Loinard, L., Dzib, S. A., et al. 2018, ApJL, 869, L33
Pagani, L., Steinacker, J., Bacmann, A., Stutz, A., & Henning, T. 2010, Sci, 329, 1622
Pendleton, Y. J. 1994, in ASP Conf. Ser. 58, The First Symposium on the Infrared Cirrus and Diffuse Interstellar Clouds, ed. R. M. Cutri & W. B. Latter (San Francisoc, CA: ASP), 255
Perotti, G., Rocha, W. R. M., Jørgensen, J. K., et al. 2020, A&A, 643, A48
Pontoppidan, K. M., van Dishoeck, E. F., & Dartois, E. 2004, A&A, 426, 925
Qasim, D., Chuang, K. J., Fedoseev, G., et al. 2018, A&A, 612, A83
Raunier, S., Chiavassa, T., Marinelli, F., Allouche, A., & Aycard, J. P. 2003, CPL, 368, 594
Rayner, J. T., Cushing, M. C., & Vacca, W. D. 2009, ApJS, 185, 289
Rayner, J. T., Toomey, D. W., Onaka, P. M., et al. 2003, PASP, 115, 362
Reiners, A., & Zechmeister, M. 2020, ApJS, 247, 11
Rieke, G. H., Rieke, M. J., & Paul, A. E. 1989, ApJ, 336, 752
Schutte, W. A., & Khanna, R. K. 2003, A&A, 398, 1049
Skrutskie, M. F., Cutri, R. M., Stiening, R., et al. 2006, AJ, 131, 1163
Tanaka, M., Sato, S., Nagata, T., & Yamamoto, T. 1990, ApJ, 352, 724
Vacca, W. D., Cushing, M. C., & Rayner, J. T. 2003, PASP, 115, 389
Van Breemen, J. M., Min, M., Chiar, J. E., et al. 2011, A&A, 526, A152
Weingartner, J. C., & Draine, B. T. 2001, ApJ, 548, 296
Whittet, D. C. B. 2003, Dust in the Galactic Environment (Bristol: IOP Publishing)
Whittet, D. C. B., Gerakines, P. A., Hough, J. H., & Shenoy, S. S. 2001, ApJ, 547, 872
Wright, E. L., Eisenhardt, P. R. M., Mainzer, A. K., et al. 2010, AJ, 140, 1868
Zhang, C. Y., Laureijs, R. J., Clark, F. O., & Wesselius, P. R. 1988, A&A, 199, 170
Zucker, C., Speagle, J. S., Schlafly, E. F., et al. 2019, ApJ, 879, 125